J. Fluid Mech. (1997), *vol.* 351, *pp.* 223–252. Printed in the United Kingdom

A method for computing unsteady fully nonlinear interfacial waves

By JOHN GRUE, HELMER ANDRÉ FRIIS, ENOK PALM AND PER OLAV RUSÅS

Mechanics Division, Department of Mathematics, University of Oslo, Norway

(Received 24 December 1996 and in revised form 4 August 1997)

We derive a time-stepping method for unsteady fully nonlinear two-dimensional motion of a two-layer fluid. Essential parts of the method are: use of Taylor series expansions of the prognostic equations, application of spatial finite difference formulae of high order, and application of Cauchy's theorem to solve the Laplace equation, where the latter is found to be advantageous in avoiding instability. The method is computationally very efficient. The model is applied to investigate unsteady transcritical two-layer flow over a bottom topography. We are able to simulate a set of laboratory experiments on this problem described by Melville & Helfrich (1987), finding a very good agreement between the fully nonlinear model and the experiments, where they reported bad agreement with weakly nonlinear Korteweg–de Vries theories for interfacial waves. The unsteady transcritical regime is identified. In this regime, we find that an upstream undular bore is generated when the speed of the body is less than a certain value, which somewhat exceeds the critical speed. In the remaining regime, a train of solitary waves is generated upstream. In both cases a corresponding constant level of the interface behind the body is developed. We also perform a detailed investigation of upstream generation of solitary waves by a moving body, finding that wave trains with amplitude comparable to the thickness of the thinner layer are generated. The results indicate that weakly nonlinear theories in many cases have quite limited applications in modelling unsteady transcritical two-layer flows, and that a fully nonlinear method in general is required.

1. Introduction

In 1896, Fridtjov Nansen and his crew returned from their three year journey to the Arctic Ocean. They brought to civilization a wealth of scientific observations and descriptions of unexplained natural phenomena; one of them was the dead water problem. Nansen discussed his observations on this phenomenon with Vilhelm Bjerknes, who attributed the wave resistance to internal waves generated by the ship, at the interface separating a layer of fresh water and heavier salt water. Today, one hundred years after the FRAM expedition, knowledge of flows due to internal waves, their origin and propagation is important in many connections, in addition to the dead water problem. Relevant examples are flows in fjords and at sills, breaking of internal waves and mixing processes in the ocean, motion in coastal water and sub-surface waves in a layered ocean. An important aspect of the latter relates to oil exploration in deep water, with operations performed from ships or oil platforms floating at the sea surface, connected to subsea drilling or production via long cables. Knowledge of currents in the ocean, which may be induced by internal waves, may be of importance

for the design of such constructions, in addition to the wave and current effects at the ocean surface. Dynamics of internal waves is also important in dimensioning of submerged floating tunnels, which have been proposed across Norwegian fjords. Further description of the scientific results of the FRAM expedition may be found in Eliassen (1982).

This study is in particular motivated by needs relating to the two latter problems. We want to investigate propagation properties of internal waves, their generation and interaction with a bottom topography or a submerged body in the ocean; our formulation is therefore unsteady. Observations in nature, see e.g. Farmer & Smith (1980), Apel *et al.* (1985), and laboratory experiments, see e.g. Koop & Butler (1981), Melville & Helfrich (1987), show that internal or interfacial waves may have quite large amplitudes due to the relatively small differences in density, such that the flow in many cases is outside the range of validity of weakly nonlinear theories. Motivated by these and similar observations our formulation is fully nonlinear.

To simplify the problem we consider two-dimensional flow of a two-layer fluid. This enables us to derive a time-stepping procedure using a pseudo-Lagrangian method, where at each time step the position of the interface and the quantity $\phi_1 - \mu\phi_2$ are found, where ϕ_1 and ϕ_2 denote the velocity potentials in the lower and upper layer, respectively, and $\mu = \rho_2/\rho_1$, where ρ denotes the corresponding fluid density. The discrete versions of the prognostic equations are obtained by Taylor series expansions including several terms, as advocated by Dold & Peregrine (1985) and Dold (1992), who studied nonlinear free surface flows. This leads to very efficient computations.

The Eulerian velocity fields in the layers are obtained by solving the Laplace equation at each time step. It turns out that accurate solution of the Laplace equation is crucial to an algorithm for computing interfacial flows. Earlier works on the time evolution of nonlinear interfacial flows have applied singularity distributions along the interface to solve the Laplace equation, see e.g. Baker, Meiron & Orszag (1982), Roberts (1983), Zhou & Graebel (1990) and Eliassen & Fjørtoft (1992). During the development of the present method we have investigated the performance of vortex or dipole distributions, but encountered problems due to numerical instability of the solution even for moderate nonlinearity of the waves. This was also the conclusion of the algoritm described by Baker *et al.* (1982), and, at the onset, of the algorithm described by Roberts (1983). Roberts was, however, able to make modifications to the scheme which removed the instabilities in his investigations. We have found it advantageous to seek a different method than using singularity distributions directly to solve the Laplace equation, and have chosen to employ Cauchy's integral theorem for this purpose. This method has been applied in several works on the evolution of nonlinear free surface waves, see e.g. Vinje & Brevig (1981), Dold & Peregrine (1985), Schultz, Huh & Griffin (1994) and references cited therein, and is reported to give less problems with regard to numerical instability than other algorithms developed for flows with free boundaries. We find that this is true also for computations of interfacial waves, which is partly explained by a stability analysis (§3.2), where we find that our scheme is neutrally stable for linear flows.

The physical Kelvin–Helmholtz instability, which is inherent to any transient interface method once the wave amplitude becomes finite, makes modelling of interfacial waves fundamentally different from free surface waves, however. This instability represents a difficulty since the time simulations become unstable to space disturbances shorter than a certain threshold value, and then tend to break down. We shall avoid the Kelvin–Helmholtz instability in the present formulation. This means that an ac-

curate solution of the Laplace equation with a moderately fine space discretization is important.

While Baker *et al.* (1982) basically used their method to simulate free surface flows, Roberts (1983) simulated steadily progressing interfacial waves, and Eliassen & Fjørtoft (1992) computed interfacial waves and roll-up of vortices developing from an initial disturbance. Their method was also formulated for flows in three dimensions.

Here, we apply the model to investigate transcritical two-layer flow over a bottom topography. This issue has been studied by means of hydraulic nonlinear theory or weakly nonlinear dispersive models (Baines 1984; Grimshaw & Smyth 1986; Miles 1979, 1981; Melville & Helfrich 1987; Zhu, Wu & Yates 1987), assuming that the amplitude is small, which, however, may be a severe restriction in many cases. We are able to simulate a set of laboratory experiments described by Melville & Helfrich (1987) on transcritical flow, which to our knowledge have not yet been confirmed by theoretical and numerical models. In this set of experiments, where the elevation of the interface is rather large, we find a striking agreement between the fully nonlinear model and the experiments, where severe disagreement with weakly nonlinear Korteweg–de Vries (KdV) theories for interfacial waves was reported. Furthermore, we investigate the upstream generation of solitary waves when the depth ratio between the two fluids is 1 to 4. In all cases here we find that trains of solitary waves with amplitudes comparable to the thickness of the thinner layer are generated, irrespective of the nonlinearity of the forcing (the volume under the geometry cannot be too small). This means that weakly nonlinear theories are inadequate in the examples considered.

Upstream influence in a two-layer fluid has its counterpart in free surface flows, see e.g. Wu (1987) and Casciola & Landrini (1996) and the references therein. In the latter paper the evolution of long waves on the surface of a one-layer fluid is considered, and fully nonlinear simulations are compared with those of Boussinesq and KdV models. Casciola & Landrini find that weakly nonlinear models in most cases capture most of the features observed in the fully nonlinear solutions of forced long waves (except close to wave breaking). This is fundamentally different from what we find here for a two-layer fluid with $(\rho_1 - \rho_2)/\rho_1$ small.

The literature on nonlinear internal waves is rather extensive. The first works date back to Keulegan (1953) and Long (1956) who investigated interfacial solitary wave solutions exploiting weakly nonlinear Boussinesq equations and the KdV equation, finding sech^2-profiles. Benjamin (1967) investigated weakly nonlinear internal waves when one of the layers is infinitely deep, also allowing for a continuous stratification, finding solitary waves of algebraic form. He also investigated flows due to two infinite layers of different, but constant, densities separated by an intermediate layer where the density can vary. The latter problem was at the same time considered by Davis & Acrivos (1967). Later Ono (1975) generalized the work of Benjamin to include unsteady behaviour of algebraic solitary waves, deriving an equation which later was termed the Benjamin–Ono (BO) equation. To bridge the gap between the shallow water and the BO equations Joseph (1977) and Kubota, Ko & Dobbs (1978) derived a formulation, which is termed 'the finite-depth theory'.

During the past couple of decades several works have been published on strongly nonlinear periodic progressive waves, which for sufficiently large amplitude may be overhanging (Holyer 1979; Vanden-Broeck 1980; Meiron & Saffman 1983; Turner & Vanden-Broeck 1986). There are also several works on strongly nonlinear interfacial solitary waves, which, like periodic waves, may be overhanging for large amplitude, see e.g. Pullin & Grimshaw (1988). Furthermore, solitary waves are found to have broadening effect due to the limited depth of the thicker layer (Amick & Turner

1986; Turner & Vanden-Broeck 1988). We have used our method to recompute weakly nonlinear interfacial waves, steep periodic wave trains and nonlinear solitary waves, arriving at the results described in the cited works.

It is relevant to mention the rather broad activity on internal waves, see e.g. Staquet & Sommeria (1996).

The paper is organized as follows. In §2 the mathematical formulation is given, including a description of the time-stepping procedure and the solution procedure of the Laplace equation. (We note that §2.2 describing the time-stepping procedure in many steps is necessarily quite similar to the descriptions by Roberts (1983), Zhou & Graebel (1990) and Eliassen & Fjørtoft (1992).) Section 3 describes the numerical implementation, stability, accuracy and convergence of the method, and how we prevent breakdown of the simulations, which can be caused by the physical Kelvin–Helmoltz instability in flows with a finite velocity jump at the interface. Further details of the method may be found in Friis (1995). In §4 we compare fully nonlinear solitary wave solutions with available experiments and weakly nonlinear theories. Section 5 is devoted to transcritical two-layer flow over a bottom topography, upstream influence and generation of solitary waves. Finally, §6 is a conclusion.

2. Mathematical formulation

2.1. *The boundary value problem*

We consider two-dimensional motion of two fluid layers of infinite horizontal extent under the action of gravity, with the gravitation force along the negative vertical direction. The lower fluid layer has thickness h_1 at rest and constant density ρ_1, and the upper layer has thickness h_2 at rest and constant density ρ_2, where ρ_2 is smaller than ρ_1. Hereafter, index 1 refers to the lower fluid, and index 2 to the upper. A coordinate system O, xy is introduced with the x-axis along the interface at rest and the y-axis pointing upwards. Unit vectors $\boldsymbol{i}, \boldsymbol{j}$ are introduced accordingly. We assume that the two fluids are homogeneous and incompressible and that the motion in each of the layers is irrotational such that the velocities may be obtained by potential theory, i.e.

$$\boldsymbol{v}_1 = u_1\boldsymbol{i} + v_1\boldsymbol{j} = \nabla\phi_1, \quad \boldsymbol{v}_2 = u_2\boldsymbol{i} + v_2\boldsymbol{j} = \nabla\phi_2, \tag{1}$$

where ϕ_1 and ϕ_2 satisfy the Laplace equation in their respective domains.

The kinematic boundary condition at the interface I separating the fluids is given by

$$\frac{\partial\phi_1}{\partial n} = \frac{\partial\phi_2}{\partial n} = V_n \quad \text{at} \quad I \tag{2}$$

where $\partial/\partial n$ means differentiation along the unit normal $\boldsymbol{n}$ of the interface and V_n is the normal velocity of the interface along $\boldsymbol{n}$. The dynamic boundary condition at the interface is obtained by balancing the pressure difference with the interfacial tension, giving

$$p_1 - p_2 = \frac{\sigma}{R_I} \quad \text{at} \quad I. \tag{3}$$

Here σ denotes the coefficient of interfacial tension, R_I the radius of curvature of the interface being positive when drawn into fluid 1, and the pressure in each of the layers is given by the Bernoulli equation, i.e.

$$\frac{p_j}{\rho_j} + \frac{\partial\phi_j}{\partial t} + \tfrac{1}{2}\boldsymbol{v}_j^2 + gy = 0, \quad j = 1, 2. \tag{4}$$

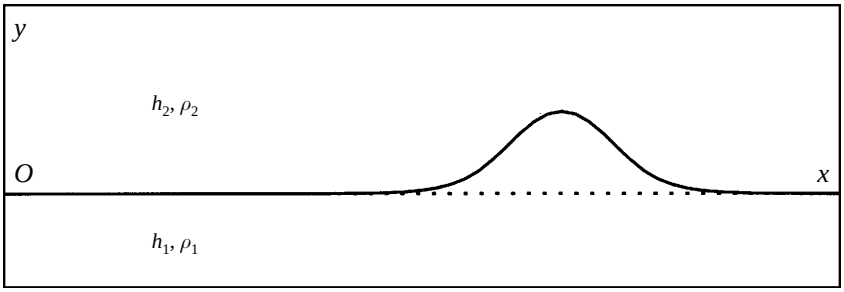

FIGURE 1. Two-dimensional interfacial flow.

We shall account in the model for a restrained or moving body in one of the fluids. Here we develop the equations for a body in the lower layer, but note that the equations may easily be modified to also account for a body in the upper layer. For a (rigid) body moving with translatory velocity $\boldsymbol{V}$, the kinematic condition at its boundary B gives

$$\frac{\partial \phi_1}{\partial n} = \boldsymbol{V} \cdot \boldsymbol{n} \quad \text{at} \quad B. \tag{5}$$

If $\boldsymbol{V} = 0$, $\partial \phi_1 / \partial n = 0$ at B. The lower boundary of layer 1, outside a possible body, is horizontal, and the kinematic boundary condition there gives

$$\frac{\partial \phi_1}{\partial y} = 0 \quad \text{at} \quad y = -h_1. \tag{6}$$

As boundary condition on top of the upper fluid, which in realistic problems is a free surface, we may in the cases under investigation justify the simplifying rigid lid approximation, i.e.

$$\frac{\partial \phi_2}{\partial y} = 0 \quad \text{at} \quad y = h_2. \tag{7}$$

To close the boundary value problem the motion is assumed to be either periodic in the x-direction or disappear for $x \to \pm\infty$.

A schematic view of the problem is shown in figure 1.

2.2. *Time-stepping procedure*

A time-stepping procedure for the interface and the flow in the fluids may be derived using the kinematic and dynamic boundary conditions at the interface. We adopt a Lagrangian method where pseudo-Lagrangian particles are introduced on the interface, each with a weighted velocity $\boldsymbol{v}_\times$ defined by

$$\boldsymbol{v}_\times = (1 - \alpha)\boldsymbol{v}_1 + \alpha \boldsymbol{v}_2, \tag{8}$$

where $\boldsymbol{v}_\times \cdot \boldsymbol{n} = V_n$ and $0 \leqslant \alpha \leqslant 1$. A pseudo-particle coincides with a particle at the interface in the lower fluid if $\alpha = 0$, and with a particle at the interface in the upper fluid if $\alpha = 1$. We have applied different values of α in testing the method and find that the best performance is achieved when α is chosen such that a typical horizontal velocity of the pseudo-particles is as small as possible. (α is a constant in each of the time simulations.) A pseudo-Lagrangian derivative is next introduced by

$$\frac{\mathrm{D}_\times}{\mathrm{d}t} = \frac{\partial}{\partial t} + \boldsymbol{v}_\times \cdot \nabla. \tag{9}$$

To determine the position $\boldsymbol{R} = (X, Y)$ of a pseudo-particle we have the following relation:

$$\frac{\mathrm{D}_\times \boldsymbol{R}}{\mathrm{d}t} = \boldsymbol{v}_\times. \tag{10}$$

We next consider the dynamic boundary condition at the interface. The pressure in the fluids may be written by means of (9)

$$\frac{p_j}{\rho_j} + \frac{\mathrm{D}_\times \phi_j}{\mathrm{d}t} - \boldsymbol{v}_\times \cdot \boldsymbol{v}_j + \tfrac{1}{2}\boldsymbol{v}_j^2 + gy = 0. \quad j = 1, 2, \tag{11}$$

Introducing (11) into the dynamic boundary condition (3) we find

$$\frac{\mathrm{D}_\times(\phi_1 - \mu\phi_2)}{\mathrm{d}t} = \boldsymbol{v}_\times \cdot (\boldsymbol{v}_1 - \mu\boldsymbol{v}_2) - \tfrac{1}{2}(\boldsymbol{v}_1^2 - \mu\boldsymbol{v}_2^2) - (1-\mu)gY - \frac{\sigma}{\rho_1 R_I} \quad \text{at} \quad I, \tag{12}$$

where $\mu = \rho_2/\rho_1$. This motivates introducing at the interface I

$$\psi = \phi_1 - \mu\phi_2. \tag{13}$$

For later use (see §2.3) we also introduce

$$\Upsilon = \phi_1 + \phi_2 \tag{14}$$

and derive equations for ψ, Υ_ξ and $\phi_{1v} = \phi_{2v}$ at the interface, where the ξ- and v-variables are defined after (26), and thereafter find $\phi_{1\xi}$ and $\phi_{2\xi}$ from

$$\phi_{1\xi} = \frac{1}{1+\mu}(\psi_\xi + \mu\Upsilon_\xi), \tag{15}$$

$$\phi_{2\xi} = \frac{1}{\mu}(\phi_{1\xi} - \psi_\xi). \tag{16}$$

Equations (10) and (12) contain sufficient information to integrate $\boldsymbol{R}$ and ψ forward in time. It is, however, an advantage also to apply higher-order derivatives of (10) and (12) in a time-stepping procedure for $\boldsymbol{R}$ and ψ. Following Dold & Peregrine (1985), who studied free surface waves, the prognostic equations for $\boldsymbol{R}$ and ψ are obtained by Taylor series expansions, as follows:

$$\boldsymbol{R}(t+\Delta t) = \boldsymbol{R}(t) + \boldsymbol{v}_\times(t)\Delta t + \frac{1}{2!}\frac{\mathrm{D}_\times \boldsymbol{v}_\times}{\mathrm{d}t}(t)(\Delta t)^2 + \frac{1}{3!}\frac{\mathrm{D}_\times^2 \boldsymbol{v}_\times}{\mathrm{d}t^2}(t)(\Delta t)^3 + \ldots, \tag{17}$$

$$\psi(t+\Delta t) = \psi(t) + \frac{\mathrm{D}_\times \psi}{\mathrm{d}t}(t)\Delta t + \frac{1}{2!}\frac{\mathrm{D}_\times^2 \psi}{\mathrm{d}t^2}(t)(\Delta t)^2 + \frac{1}{3!}\frac{\mathrm{D}_\times^3 \psi}{\mathrm{d}t^3}(t)(\Delta t)^3 + \ldots, \tag{18}$$

This procedure has an error of the order $(\Delta t)^{n+1}/(n+1)!$ at each time step when terms up to the nth derivative are included in the expansions, which is an essential improvement compared to an algorithm based on first-derivatives only. In the computations we truncate the series after $n = 7$. Procedures for how to evaluate $\mathrm{D}_\times^m \boldsymbol{v}_\times/\mathrm{d}t^m$ ($m = 1, \ldots, 6$) and $\mathrm{D}_\times^m \psi/\mathrm{d}t^m$ ($m = 1, \ldots, 7$) are described at the end of §2.3 and in Appendix A.

2.3. *Solution of the Laplace equation*

As noted in the Introduction, accurate solution of the Laplace equation is crucial to an algorithm for computing interfacial flows, and we here apply Cauchy's integral theorem for this purpose. Invoking complex analysis we introduce the complex variable $z = x + \mathrm{i}y$ and complex velocities $q_j(z) = u_j - \mathrm{i}w_j$, $j = 1, 2$. Since q_j are

analytic functions of z, we have by use of Cauchy's integral theorem for z' outside the respective fluid layer

$$\oint_{C_1} \frac{q_1 \mathrm{d}z}{z - z'} = 0, \quad \oint_{C_2} \frac{q_2 \mathrm{d}z}{z - z'} = 0. \tag{19}$$

The contours C_j ($j = 1, 2$) are composed of the interface, the rigid horizontal boundaries of the fluid layers, and C_1 contains the contour of the body geometry. In addition, C_j contains vertical boundaries, either in accordance with the periodicity of the flow, or at infinity. The integrals over these parts of C_j vanish due to the conditions described in §2.1 after (7). The integration is clockwise along C_1 and counterclockwise along C_2.

The rigid wall conditions (6) and (7) at $y = -h_1, h_2$ are accounted for by applying the method of images. For a point z at the interface, the images about the rigid walls at $y = -h_1$ and $y = h_2$ are given by, respectively,

$$\tilde{z}_1 = z^* - 2\mathrm{i}h_1, \quad \tilde{z}_2 = z^* + 2\mathrm{i}h_2, \tag{20}$$

where a star denotes a complex conjugate. Analytical continuation of the complex velocities outside the rigid boundaries of the respective fluid domains are obtained from

$$q_j(\tilde{z}_j) = q_j^*(z) = u_j(x, y) + \mathrm{i}v_j(x, y). \tag{21}$$

Equation (19) then gives

$$\int_I \frac{q_2(z)\mathrm{d}z}{z - z'} - \int_I \frac{q_2^*(z)\mathrm{d}z^*}{z^* + 2\mathrm{i}h_2 - z'} = 0, \tag{22}$$

$$\int_{I+B} \frac{q_1(z)\mathrm{d}z}{z - z'} - \int_{I+B} \frac{q_1^*(z)\mathrm{d}z^*}{z^* - 2\mathrm{i}h_1 - z'} = 0. \tag{23}$$

Letting z' approach I and B from outside each of the fluids and applying the Plemelj formula we obtain from (22)–(23):

$$-\pi \mathrm{i} q_2(z') = \mathrm{PV} \int_I \frac{q_2(z)\mathrm{d}z}{z' - z} + \int_I \frac{q_2^*(z)\mathrm{d}z^*}{z^* + 2\mathrm{i}h_2 - z'} \quad (z' \text{ on } I), \tag{24}$$

$$\pi \mathrm{i} q_1(z') = \mathrm{PV} \int_I \frac{q_1(z)\mathrm{d}z}{z' - z} + \int_I \frac{q_1^*(z)\mathrm{d}z^*}{z^* - 2\mathrm{i}h_1 - z'} + \int_B \frac{q_1(z)\mathrm{d}z}{z' - z} + \int_B \frac{q_1^*(z)\mathrm{d}z^*}{z^* - 2\mathrm{i}h_1 - z'} \quad (z' \text{ on } I) \tag{25}$$

$$\pi \mathrm{i} q_1(z') = \int_I \frac{q_1(z)\mathrm{d}z}{z' - z} + \int_I \frac{q_1^*(z)\mathrm{d}z^*}{z^* - 2\mathrm{i}h_1 - z'} + \mathrm{PV} \int_B \frac{q_1(z)\mathrm{d}z}{z' - z} + \int_B \frac{q_1^*(z)\mathrm{d}z^*}{z^* - 2\mathrm{i}h_1 - z'} \quad (z' \text{ on } B) \tag{26}$$

where PV denotes principal value. Only the real part of the principal value integrals in (24)–(26) are singular.

Following the method by Dold & Peregrine (1985) for free surface flows, we introduce a ξ-variable as coordinate along the interface, and tangential and normal derivatives of the potentials at I and B by

$$q_j = (\phi_{js} - \mathrm{i}\phi_{jn}) z_s^* = (\phi_{j\xi} - \mathrm{i}\phi_{jv}) \frac{z_\xi^*}{|z_\xi|^2}, \quad j = 1, 2 \tag{27}$$

where $(\ )_s = \partial/\partial s$ denotes differentiation along the arclength s of I, $(\ )_n = \partial/\partial n$, $(\ )_\xi = \partial/\partial\xi$ and $(\ )_v = \partial/\partial v$. We hereafter work with the scaled tangential and normal velocities $\phi_{j\xi} = \phi_{js}|z_\xi|$ and $\phi_{jv} = \phi_{jn}|z_\xi|$.

We then subtract (24) from (25), multiply by z'_ξ and apply (27). From the imaginary part of the result we obtain the following equation for $\Upsilon_\xi = \phi_{1\xi} + \phi_{2\xi}$:

$$\begin{aligned}\pi\Upsilon_\xi(\xi') = {} & \frac{2}{\mu+1}\int_I \mathrm{Im}\left(\frac{z'_\xi}{z'-z}\right)\psi_\xi \mathrm{d}\xi + \frac{\mu-1}{\mu+1}\int_I \mathrm{Im}\left(\frac{z'_\xi}{z'-z}\right)\Upsilon_\xi \mathrm{d}\xi \\ & + \int_I \mathrm{Re}\left(\frac{z'_\xi}{z^*-2\mathrm{i}h_1-z'} - \frac{z'_\xi}{z^*+2\mathrm{i}h_2-z'}\right)\phi_{1v}\mathrm{d}\xi \\ & + \frac{1}{1+\mu}\int_I \mathrm{Im}\left(\frac{z'_\xi}{z^*-2\mathrm{i}h_1-z'} + \frac{z'_\xi}{z^*+2\mathrm{i}h_2-z'}\right)\psi_\xi \mathrm{d}\xi \\ & + \frac{1}{1+\mu}\int_I \mathrm{Im}\left(\mu\frac{z'_\xi}{z^*-2\mathrm{i}h_1-z'} - \frac{z'_\xi}{z^*+2\mathrm{i}h_2-z'}\right)\Upsilon_\xi \mathrm{d}\xi \\ & + \int_B \mathrm{Re}\left(-\frac{z'_\xi}{z'-z} + \frac{z'_\xi}{z^*-2\mathrm{i}h_1-z'}\right)\phi_{1v}\mathrm{d}\xi \\ & + \int_B \mathrm{Im}\left(\frac{z'_\xi}{z'-z} + \frac{z'_\xi}{z^*-2\mathrm{i}h_1-z'}\right)\phi_{1\xi}\mathrm{d}\xi \end{aligned} \tag{28}$$

for z' on I. To obtain (28) we have also used the kinematic condition (2) at the interface. We note that (28) does not contain principal value integrals.

Next, multiplying (24) and (25) by z'_ξ and taking the real part, we may combine the resulting equations to give

$$\begin{aligned}\pi(1+\mu)\phi_{1v}(\xi') = {} & \mathrm{PV}\int_I \mathrm{Re}\left(\frac{z'_\xi}{z'-z}\right)\psi_\xi \mathrm{d}\xi + (1-\mu)\int_I \mathrm{Im}\left(\frac{z'_\xi}{z'-z}\right)\phi_{1v}\mathrm{d}\xi \\ & + \frac{1}{1+\mu}\int_I \mathrm{Re}\left(\frac{z'_\xi}{z^*-2\mathrm{i}h_1-z'} + \mu\frac{z'_\xi}{z^*+2\mathrm{i}h_2-z'}\right)\psi_\xi \mathrm{d}\xi \\ & + \frac{\mu}{1+\mu}\int_I \mathrm{Re}\left(\frac{z'_\xi}{z^*-2\mathrm{i}h_1-z'} - \frac{z'_\xi}{z^*+2\mathrm{i}h_2-z'}\right)\Upsilon_\xi \mathrm{d}\xi \\ & - \int_I \mathrm{Im}\left(\frac{z'_\xi}{z^*-2\mathrm{i}h_1-z'} - \mu\frac{z'_\xi}{z^*+2\mathrm{i}h_2-z'}\right)\phi_{1v}\mathrm{d}\xi \\ & + \int_B \mathrm{Re}\left(\frac{z'_\xi}{z'-z} + \frac{z'_\xi}{z^*-2\mathrm{i}h_1-z'}\right)\phi_{1\xi}\mathrm{d}\xi \\ & + \int_B \mathrm{Im}\left(\frac{z'_\xi}{z'-z} - \frac{z'_\xi}{z^*-2\mathrm{i}h_1-z'}\right)\phi_{1v}\mathrm{d}\xi \end{aligned} \tag{29}$$

for z' on I, where (2) is applied.

Finally, multiplying (26) by z'_ξ and taking the imaginary part, we obtain

$$\begin{aligned}\pi\phi_{1\xi}(\xi') = {} & \int_I \mathrm{Re}\left(-\frac{z'_\xi}{z'-z} + \frac{z'_\xi}{z^*-2\mathrm{i}h_1-z'}\right)\phi_{1v}\mathrm{d}\xi \\ & + \frac{1}{1+\mu}\int_I \mathrm{Im}\left(\frac{z'_\xi}{z'-z} + \frac{z'_\xi}{z^*-2\mathrm{i}h_1-z'}\right)\psi_\xi \mathrm{d}\xi \\ & + \frac{\mu}{1+\mu}\int_I \mathrm{Im}\left(\frac{z'_\xi}{z'-z} + \frac{z'_\xi}{z^*-2\mathrm{i}h_1-z'}\right)\Upsilon_\xi \mathrm{d}\xi \end{aligned}$$

$$+\mathrm{PV}\int_B \mathrm{Re}\left(-\frac{z'_\xi}{z'-z}+\frac{z'_\xi}{z^*-2\mathrm{i}h_1-z'}\right)\phi_{1v}\mathrm{d}\xi$$
$$+\int_B \mathrm{Im}\left(\frac{z'_\xi}{z'-z}+\frac{z'_\xi}{z^*-2\mathrm{i}h_1-z'}\right)\phi_{1\xi}\mathrm{d}\xi \tag{30}$$

for z' on B.

Equations (28)–(30) determine Υ_ξ and ϕ_{1v} at the interface I and $\phi_{1\xi}$ at the body B, since ψ on I and ϕ_{1v} on B are given. The velocities on both sides of the interface are finally found from (15), (16), (27). If the body is entirely surrounded by fluid, we must also specify the circulation around B, i.e.

$$\int_B \phi_{1\xi}(\xi)\mathrm{d}\xi = 0 \tag{31}$$

which gives an additional equation.

We are now able to evaluate the terms containing the first derivatives in (17)–(18). In order to obtain the second- and third-order pseudo-Lagrangian derivatives of $\boldsymbol{R}$ and ψ, we need to compute $\partial q_j/\partial t$ and $\partial^2 q_j/\partial t^2$, which, by exploiting their analyticity, may be found from Cauchy's theorem, giving the same integral equations (24)–(26) as for the velocities q_j. Similar integral equations for $\partial\phi_{1v}/\partial t$, $\partial\Upsilon_\xi/\partial t$ and $\partial^2\phi_{1v}/\partial t^2$, $\partial^2\Upsilon_\xi/\partial t^2$ may be constructed by exploiting the relevant boundary conditions at the interface; the details are given in Appendix A. Pseudo-derivatives of order four to seven are obtained by backwards differencing in time, based on the third-order pseudo-derivatives.

2.4. *The Boussinesq approximation*

When computing interfacial waves in e.g. the ocean, where μ is close to 1, we may apply the Boussinesq approximation. We then keep $1-\mu=\epsilon$ in the bouyancy term of (12), but put $\mu=1$ in all other terms. For the particular choice $\alpha=1/2$ in (8) we then obtain

$$\frac{\mathrm{D}_\times \boldsymbol{R}}{\mathrm{d}t}=\boldsymbol{v}_\times, \quad \frac{\mathrm{D}_\times \psi}{\mathrm{d}t}=-\epsilon g Y+\frac{\sigma}{\rho R_I} \quad \text{at} \quad I. \tag{32}$$

The equations for determining Υ_ξ and ϕ_{1v} also become simplified. In particular, for $h_1=h_2=\infty$ and no body present in the fluid, we obtain

$$\Upsilon'_\xi=\frac{1}{\pi}\int_I \mathrm{Im}\left(\frac{z'_\xi}{z'-z}\right)\psi_\xi\mathrm{d}\xi, \quad \phi'_{1v}=\frac{1}{2\pi}\mathrm{PV}\int_I \mathrm{Re}\left(\frac{z'_\xi}{z'-z}\right)\psi_\xi\mathrm{d}\xi \tag{33}$$

which are valid for a nonlinear interface, and mean that Υ_ξ and ϕ_{1v} are determined by integrals of (the given) ψ_ξ. This was also noted by Eliassen & Fjørtoft (1992).

This result is in contrast to modelling nonlinear free surface waves ($\mu=0$) in infinite water depth, where a set of equations must be solved to determine ϕ_{1v} at each time step.

When h_1 and h_2 are finite, the Boussinesq approximation is still better, since fewer iterations are required in the solution procedure than when $\mu\neq 1$, see §3.1.

3. Numerical aspects of the method

3.1. *Implementation*

The functions in the problem are assumed to be smooth along the boundaries and at any point within the fluids. We discretize the interface by N pseudo-Lagrangian

points and the body by N_B points, where ξ takes integer values at each point, i.e. $\xi = 1, 2, \ldots, N$ at I and $\xi = 1, 2, \ldots, N_B$ at B. The integrals are approximated by the trapezoidal rule. This integration rule gives a spectrally accurate numerical integration, i.e. the error is exponentially small, when the integrand is periodic and has sufficiently smooth derivatives, see e.g. Shelley (1992). We find that the trapezoidal rule is well suited to the problems considered here. Following Dold & Peregrine (1985), the principal value integrals are evaluated by first expanding the integrand in a series in the vincity of the pole at $z = z'$, and then carrying out the integration. For a smooth real function f we have

$$\mathrm{PV}\int_0^N \frac{z'_\xi}{z' - z(\xi)} f(\xi)\mathrm{d}\xi = \sum_{\xi=1}^{N} [\mathscr{A}(\xi', \xi) + \mathrm{i}\mathscr{B}(\xi', \xi)] f(\xi) - f_\xi(\xi'), \tag{34}$$

where

$$\mathscr{A} + \mathrm{i}\mathscr{B} = \begin{cases} z'_\xi/(z' - z), & z \neq z' \\ z_{\xi\xi}/2z_\xi, & z = z'. \end{cases} \tag{35}$$

The accuracy of the integration in (34) is determined by applying the numerical differentiation formula. In most of the computations we apply a 10-point finite difference formula based on a tenth-order polynomial expansion with an error of order $|\Delta \boldsymbol{R}|^{10}$. In the case of periodic motion we also in some examples obtain the derivatives from truncated Fourier series, giving the derivatives and the approximation to the integral in (34) with spectral accuracy. The discrete forms of the integral equations (28), (29) and (30) are given in Appendix B.

To solve the equations we first invert (30) by Gaussian elimination, expressing $\phi_{1\xi}$ at B by the unknowns $\phi_{1\nu}$ and Υ_ξ at I. Equations (28)–(29) are then solved by iteration using the generalized conjugate residuals method, which is both robust and efficient. The organization of the equations for the unknowns at the interface on the form (28)–(29) is an efficient solution procedure. In order to minimize the round-off error, all computations are performed by double-precision arithmetic.

As described in §2.2 we use expansions (17)–(18) to step $\boldsymbol{R}$ and ψ forward in time, where derivatives up to the third order are obtained from a combination of analytical formulae and solution of the integral equations. Further derivatives are found by use of four orders of backwards differencing. During the first 5 time steps of the computation the order of the backward differencing polynomial is gradually increased from 0 to 4. The time steps are small in the beginning of the computations, and are gradually increased up to a constant value Δt.

In all numerical examples presented we neglect the interfacial tension, i.e. $\sigma = 0$ in the computations.

A regridding algorithm is applied to the pseudo-particles in order to maintain an even distance between the node points at the interface during the calculations.

Mostly because of the Kelvin–Helmholtz instability (see §3.3) smoothing is required in order to maintain a stable solution. We use two smoothing formulae which are both based on a 15-point interpolation polynomial: one smooths 2-point periodic (sawtooth) disturbances from the grid, the other removes both 3-point and 2-point periodic disturbances. Both smoothing formulae remove very little energy from the waves.

3.2. *Stability of the linearized scheme; dispersion relation*

It is of interest to investigate the stability and the dispersion relation of the linearized scheme. We consider periodic perturbations Y, ϕ_1, ϕ_2, satisfying the linear versions

of (2), (10) and (12) (with $\sigma = 0$) at $y = 0$, i.e.

$$\frac{\partial Y}{\partial t} = \frac{\partial \phi_1}{\partial y}, \quad \frac{\partial \psi}{\partial t} + (1-\mu) g Y = 0. \tag{36}$$

There is no geometry in the fluids and we set $h_1 = h_2 = \infty$. From the integral equation (29) we find

$$\pi(1+\mu)\frac{\partial \phi_1}{\partial y} = -\mathrm{PV}\int_{-\infty}^{\infty} \frac{\psi_x}{x - x'}\mathrm{d}x \tag{37}$$

where the principal value integral is the double-sided Hilbert transform of ψ_x. By combining (37) with (36) we find

$$\frac{\partial^2 \psi}{\partial t^2} = \frac{g(1-\mu)}{\pi(1+\mu)}\mathrm{PV}\int_{-\infty}^{\infty} \frac{\psi_x}{x - x'}\mathrm{d}x. \tag{38}$$

We consider a periodic interface and discretize the interface by N points per wavelength, giving for the discrete version of (38)

$$\frac{\partial^2 \psi(\xi')}{\partial t^2} = -\frac{g(1-\mu)}{\pi(1+\mu)}(\mathscr{A}\mathscr{D}_1 - \mathscr{D}_2)\psi, \quad \xi' = 1, 2, \ldots, N \tag{39}$$

where $\mathscr{A}$ is given by the periodic version of (35) and $\mathscr{D}_1$, $\mathscr{D}_2$ denote the operators for the first and second derivatives. To investigate the stability of the numerical scheme we seek solutions of (39) on the form $\psi(x,t) = \hat{\psi}(x)\mathrm{e}^{\mathrm{i}\omega t}$ (and $Y(x,t) = \hat{Y}(x)\mathrm{e}^{\mathrm{i}\omega t}$) where $\mathrm{i}\omega = \omega_r + \mathrm{i}\omega_i$. This leads to the following eigenvalue problem

$$\omega^2 \hat{\psi} = \frac{g(1-\mu)}{\pi(1+\mu)}(\mathscr{A}\mathscr{D}_1 - \mathscr{D}_2)\hat{\psi}. \tag{40}$$

The solution of this problem, obtained by a standard method, contains a double set of N non-zero eigensolutions corresponding to linear waves with wavenumbers $k = 1, 2, \ldots, N/2$ and (eigen) frequencies $\omega = \omega_{i1}, \omega_{i2}, \ldots, \omega_{iN/2}$, which may propagate in both horizontal directions. The first set has phase shift 0, the other phase shift $\pi/2$. We find that $\omega_r = 0$ for all wavenumbers, both when the derivatives are obtained by the 10-point finite difference formula and by the truncated Fourier series, which means that the numerical scheme is neutrally stable for linear waves.

Next we consider the analytical and numerical dispersion relations of the problem, which are obtained by inserting $\psi = \mathrm{Re}(\hat{\psi}\mathrm{e}^{\mathrm{i}kx - \mathrm{i}\omega t})$ into (38) and (39) (ω denotes the frequency and k the wavenumber). Noting that the double-sided Hilbert transform of $\mathrm{e}^{\mathrm{i}kx}$ is determined by

$$\mathrm{PV}\int_{-\infty}^{\infty} \frac{\mathrm{e}^{\mathrm{i}kx}}{x - x'}\mathrm{d}x = \mathrm{i}\pi\mathrm{e}^{\mathrm{i}kx'} \tag{41}$$

we find from (38) that the analytical dispersion relation becomes

$$\omega^2 = gk(1-\mu)/(1+\mu). \tag{42}$$

When the periodic interface is discretized by N points per wavelength we obtain from (39) a numerical dispersion relation for wavenumbers up to $k = N/2$, the Nyquist wave. This dispersion relation is obtained by differencing in two ways: either by the 10-point finite difference formula or by the truncated Fourier series. Since the tapezoidal rule yields a spectrally accurate approximation to the integral in (41) (see §3.1) we expect that the latter method gives a numerical dispersion relation with spectral accuracy, as also found by the computations. We note that the various dispersion relations are independent of the value of μ, except for the prefactor on the

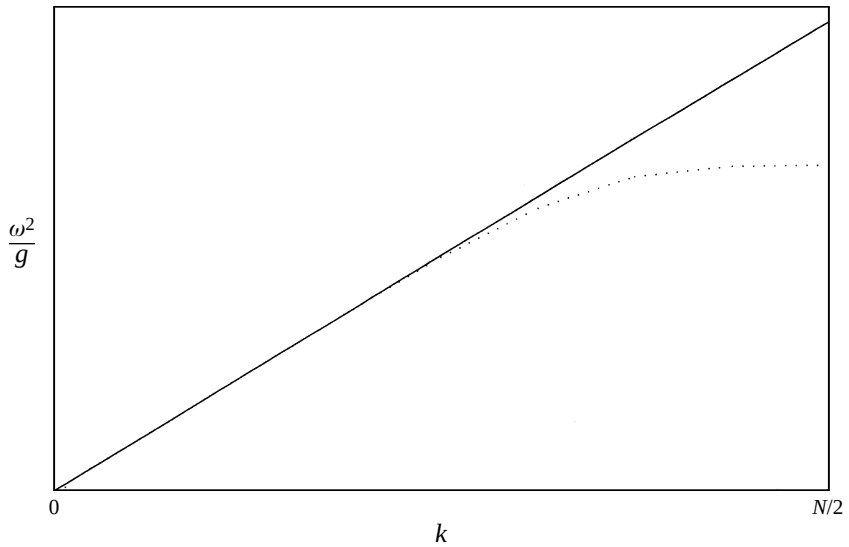

FIGURE 2. Numerical dispersion relation. Solid line: analytical (42) and spectral method. Dotted line: 10-point finite difference formula used for numerical differentiation ($\mu = 0.1$).

right of (40), which is because we for the moment have set $h_1 = h_2 = \infty$. In fact, we recover the results for free surface waves ($\mu = 0$) which is discussed by Dold (1992).

In figure 2 we show the graph of ω^2 versus k for the analytical dispersion relation (42) and the two different numerical dispersion relations. (The numerical dispersion relation corresponding to the spectral derivatives coincides with the analytical dispersion relation for $k \leqslant N/2$.) The numerical dispersion relation due to the 10-point finite difference formula coincides with the analytical dispersion relation up to $k \sim N/4$, but deviates somewhat for larger wavenumbers. This deviation is of minor importance, however, since in the numerical simulations we apply smoothing to remove short disturbances. From numerical experiments it turns out that the 10-point finite difference formula is adequate for the examples considered here.

3.3. *The effect of the Kelvin–Helmholtz instability*

When we apply the model to linear interfacial waves, we encounter no problems with regard to instability. Once the wave steepness becomes finite, however, the physical Kelvin–Helmholtz (K-H) instability due to the wave-induced velocity jump occurring at the interface is included in the model. This means that the numerical solution becomes unstable to disturbances with wavelength shorter than a threshold value, λ_{KH}, say, which prevents us from refining the space discretization below this value, if no smoothing is applied. The nonlinear computations show that λ_{KH} has a marked increase with growing velocity jump at the interface. λ_{KH} also grows with increasing $\mu = \rho_2/\rho_1$. This increase is, however, moderate when μ is larger than about 0.2, since the velocity shear due to the interfacial waves is decreasing with increasing μ.

The K-H instability due to interfacial waves in a real two-layer fluid, or a fluid with a localized vertical density variation, is in most cases limited by local nonlinearity, viscous effects and/or interfacial tension, which are effects that prevent breakdown of the large-scale wave motion. Thus, the present model, where the effect of the K-H instability is suppressed, may provide a reasonable approach to large-scale behaviour

(*a*) N	$\omega\Delta T$	$\overline{Y}/a$	$\Delta E/E$	(*b*) $\omega\Delta t$	$\overline{Y}/a$	$\Delta E/E$
20	2.0	0.00260000	0.00600000	0.5	0.0002100	0.0004000
20	1.5	0.00000860	0.00000530	0.2	0.0000027	0.0000074
20	1.0	0.00000160	0.00000170	0.1	0.0000012	0.0000024
20	0.5	0.00000180	0.00000370	0.01	0.0000016	0.0000017
30	0.5	0.00000030	0.00000015			
30	0.25	0.00000009	0.00000014			
30	0.1	0.00000014	0.00000025			
30	0.05	0.00000020	0.00000037			
60	0.1	0.00014000	0.00013000			
60	0.05	0.00000130	0.00000120			
60	0.01	0.00000002	0.00000003			

TABLE 1. (*a*) Propagation of periodic interfacial waves (wave period $2\pi/\omega$). Relative error after four wave periods in the mean interfacial level and energy E vs. discretization N and smoothing interval $\omega\Delta T$. Time step $\omega\Delta t = 0.01$. $ak = 0.345$, $\mu = 0.1$, $h_1 = h_2 = \infty$. 2-point smoothing for $N = 20$, 30; 3-point smoothing for $N = 60$. (*b*) Same as (*a*), but $\omega\Delta T = 1.0$, $N = 20$, 2-point smoothing.

of interfacial waves, as long as λ_{KH} is much smaller than the main length scales of the wave motion.

The K-H instability makes modelling of interfacial waves fundamentally different from free surface waves. This instability represents a difficulty since the space discretization in a two-layer model cannot be too fine, and convergence of transient simulations of steep waves may be difficult to document. However, we may obtain convergence when the wave amplitude is moderate (§3.4). We may also compare the waves resulting from the time simulations with steady solutions of interfacial waves, where arbitrary refinement of the discretization may be performed, providing complementary documentation of convergence (§5.4).

3.4. *Accuracy and convergence*

To measure the accuracy and the convergence of the method we investigate how wave form, volume of the wave, mean level of the interface and energy are conserved in some examples for waves propagating steadily along the interface.

The kinetic energy due to the motion in the fluid layers may, by applying the divergence theorem and the kinematic boundary conditions, be expressed as an integral along the interface. By adding the potential energy we find that the energy of the fluid motion is given by

$$E = \tfrac{1}{2}\rho_1 \int_0^N \psi(\xi)\phi_{1v}(\xi)\mathrm{d}\xi + \tfrac{1}{2}g\rho_1(1-\mu)\int_0^N Y^2(\xi)X_\xi(\xi)\mathrm{d}\xi. \tag{43}$$

The initial profile and propagating velocity c of the wave(s) are determined by applying the equations of §§2.2–2.3 in a frame of reference moving with the speed of the wave, i.e. where $\partial/\partial t = -c\partial/\partial x$. The resulting nonlinear equations are solved by means of Newton's method.

In the first example we compute periodic nonlinear interfacial waves propagating during a time interval corresponding to four wave periods. The wave data are: $ak = 0.345$ (a the wave amplitude, k the wavenumber), $\mu = 0.1$ and $h_1 = h_2 = \infty$. We show in table 1 the relative error in the mean interfacial level ($\overline{Y}$) and the energy (E), for various discretizations per wavelength (N), time step (Δt) and smoothing interval

N	$\Delta t(g/h_2)^{1/2}$	$\Delta T(g/h_2)^{1/2}$	$\Delta V/V$	$\Delta E/E$
61	0.1	5.0	0.000300	0.001000
81	0.1	3.0	0.000030	0.000090
125	0.1	1.0	0.000005	0.000005
81	3.0	3.0	0.002000	0.000900
81	1.0	3.0	0.000200	0.000010
81	0.5	3.0	0.000030	0.000090

TABLE 2. Relative error in volume V and energy E due to a solitary wave which has propagated a distance of $100h_2$. $|Y|_{max}/h_2 = 0.7$, $h_1/h_2 = 4$, $\mu = 0.9$. 2-point smoothing. The wave profile is shown in figure 4(b).

(ΔT). The table clearly demonstrates convergence of the method with respect to increasing N and decreasing Δt, that the smoothing interval ΔT cannot be too large, and that highest accuracy is obtained for relatively small ΔT. The smallest relative error in these computations is only 3×10^{-8}. The relative errors in the wave form and the propagation speed are of the same order as for $\overline{Y}$ and E. A more frequent smoothing reduce the aliasing errors in the simulations, see table 1(a) for $N = 20$ and 60.

In the next example a solitary wave is considered, with $|Y|_{max}/h_2 = 0.7$, $h_1/h_2 = 4$, $\mu = 0.9$. The interface is discretized from the wave crest and out to horizontal positions $\pm 59.5h_2$, where $|Y/h_2|$ becomes smaller than 10^{-10}. The resulting wave is shown in figure 4(b) below. Table 2 displays the relative error in volume and energy after the wave has propagated a distance $100h_2$. Again the computations show convergence of the method, and that a relatively small smoothing interval ΔT gives a high accuracy. We note though that $\Delta t/\Delta T$ always should be a small number in the computations, in order to smooth as little as possible. The smallest relative error in these computations is 5×10^{-6}.

4. Solitary waves: comparison with experiments and weakly nonlinear theories

One way of illustrating the usefulness of our fully nonlinear method is to compare solitary wave solutions with available laboratory measurements and results by asymptotic theories for such waves, i.e. the Korteweg–de Vries (KdV) theory, the Benjamin-Ono (BO) theory and the finite-depth theory, as mentioned in the Introduction. Such a comparison is also useful in the context of the findings in §5, which show that a moving body in the cases considered generates interfacial waves with amplitudes comparable to the thickness of the thinner layer.

To be specific, we briefly describe the assumptions behind these theories and present the respective formulae for solitary wave solutions. Relevant to the applications in §5 we here give formulae for $h_2 < h_1$, i.e. solitary waves with depression. Keulegan (1953) and Long (1956) considered interfacial waves in a two-layer fluid assuming that the waves are long, accounting for weak dispersion, and the amplitude small compared to the total depth of the fluid, i.e. $kH \ll 1$, $a/H \ll 1$, where k is a typical wavenumber and $H = h_1 + h_2$. These assumptions lead to the KdV equation as model for the evolution of a disturbance at the interface. The solitary wave solution for a

depression reads, in our notation (Long 1956, equations (19)–(28))

$$\eta(x-ct) = -a\,\mathrm{sech}^2[(x-ct)/\lambda], \tag{44}$$

$$\lambda^2 = \frac{4h_2^3}{3a}\,\frac{1+\rho_1 h_1/(\rho_2 h_2)}{1-\rho_1 h_2^2/(\rho_2 h_1^2)}, \tag{45}$$

$$\frac{c^2}{c_0^2} - 1 = a\,\frac{\rho_2 h_1/h_2 - \rho_1 h_2/h_1}{\rho_1 h_2 + \rho_2 h_1}, \tag{46}$$

$$c_0^2 = \frac{g h_1 h_2(\rho_1-\rho_2)}{\rho_1 h_2 + \rho_2 h_1}. \tag{47}$$

The case when $h_1 \to \infty$, $kh_2 \ll 1$ and $a/h_2 \ll 1$ (accounting for weak dispersion) was considered by Benjamin (1967, equations (5.3)–(5.7)) who found a solitary wave with algebraic decay, given by

$$\eta(x-ct) = \frac{-a}{1+(x-ct)^2/\lambda^2}, \tag{48}$$

$$\lambda = \frac{4\rho_2}{3\rho_1}\frac{h_2^2}{a}, \tag{49}$$

$$\frac{c^2}{c_0^2} - 1 = \frac{3a}{h_2}, \tag{50}$$

$$c_0^2 = \frac{\rho_1-\rho_2}{\rho_2} g h_2. \tag{51}$$

Later, Joseph (1977) and Kubota *et al.* (1978) provided a theory, termed the finite-depth theory, for the intermediate range $h_2/H \ll 1$, $kH = O(1)$, $a/h_2 \ll 1$ (accounting for weak dispersion) which includes both the KdV and the BO equations as limiting cases. A solitary wave solution was developed in the Boussinesq limit by Joseph (1977, equations (7)–(14)). According to Segur & Hammack (1982, equations (37)–(38)) this solitary wave solution may be obtained for $(\rho_1-\rho_2)/\rho_2$ not small as

$$\eta(x-ct) = \frac{-a\,\mathrm{sech}^2[(x-ct)/\lambda]}{1+\{\tan(H/\lambda)\tanh[(x-ct)/\lambda]\}^2}, \tag{52}$$

$$\lambda \cot\frac{H}{\lambda} = \frac{4\rho_2}{3\rho_1}\frac{h_2^2}{a}, \tag{53}$$

$$\frac{c}{c_0} - 1 = \frac{h_2}{2H}\left\{1 - \frac{\rho_1-\rho_2}{\rho_2}\,\frac{2H}{\lambda}\cot\left(\frac{2H}{\lambda}\right)\right\}, \tag{54}$$

$$c_0^2 = \frac{\rho_1-\rho_2}{\rho_2} g h_2. \tag{55}$$

In Koop & Butler (1981) experiments on interfacial solitary waves, using water above freon, with $\mu = 0.633$ and $h_2/h_1 = 5.086$, were compared with these asymptotic theories. Koop & Butler had, however, no fully nonlinear method available. In figure 3 we have reproduced the data set from their figure 10, displaying the half-mean elevation of solitary waves, defined by $L = \int_{-\infty}^{\infty} Y\,\mathrm{d}x/(2a)$, as a function of the maximal elevation $a = |Y|_{max}$. Due to the moderate value of h_2/h_1 we do not expect the BO equation to give good results in this comparison. The figure clearly shows

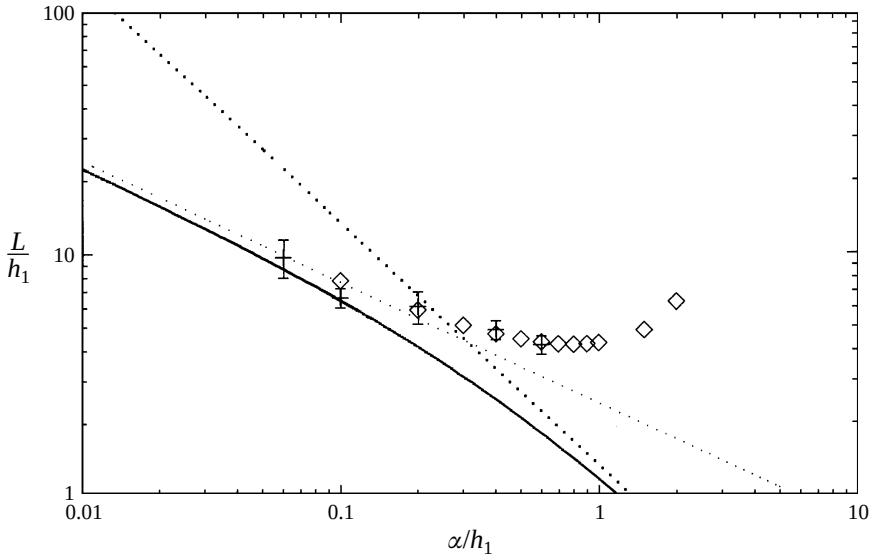

FIGURE 3. Solitary waves. Comparison between fully nonlinear theory (◇), laboratory measurements by Koop & Butler (1981, figure 10) (vertical bars), KdV theory (light dotted line), BO theory (heavy dotted line), finite-depth theory (solid line). Vertical coordinate: half-mean elevation of solitary wave. Horizontal coordinate: amplitude $a = |Y|_{max}$. $\mu = 0.633$, $h_2/h_1 = 5.086$.

that the KdV (equations (44)–(47)) and the finite-depth (equations (52)–(55)) theories have quite limited ranges of validity. In these examples the finite-depth theory is good up to a/h_1 about 0.1, while the KdV theory is relevant for somewhat larger a/h_1, up to about 0.2. Koop & Butler also provided an extension of the KdV theory, which increased its domain of validity. However, for non-dimensional amplitude of order unity, which is a relevant elevation in many applications (see also §5), the results clearly demonstrate the shortcomings of the finite-depth and the KdV theories.

In figure 3 are also displayed results obtained by the fully nonlinear method, which show excellent agreement with the experimental measurements for the whole range of a/h_1. We note that the non-dimensional area under the waves is increasing with the amplitude for $a/h_1 > 1$, which is due to the broadening effect occurring for a limited ratio between h_2 and h_1, see Amick & Turner (1986) and Turner & Vanden-Broeck (1988). For small amplitudes our method agrees with the asymptotic theories. We have performed computations in the BO case, finding close agreement with the fully nonlinear solution when $a/h_2 \leqslant 0.03$. We must then discretize the interface for $|X/h_1| < 200$ (results not shown here).

The fundamental differences between the fully nonlinear and the weakly nonlinear methods are further illustrated by the solitary wave profiles shown in figure 4, which are relevant for the applications described in the next section. In these examples $h_1/h_2 = 4$. We observe that the finite-depth, KdV and fully nonlinear methods are in approximate agreement for $|Y|_{max}/h_2$ up to about 0.15 (figure 4*a*). For non-dimensional amplitude of order unity, however, the differences between the methods become remarkably large. Both the finite-depth theory and the KdV theory now predict quite unrealistic wave shapes.

These remarkable differences have motivated us to set up experiments at the University of Oslo with the purpose of a general comparison with theory and to broaden our understanding of propagation properties of internal waves. The experiments are

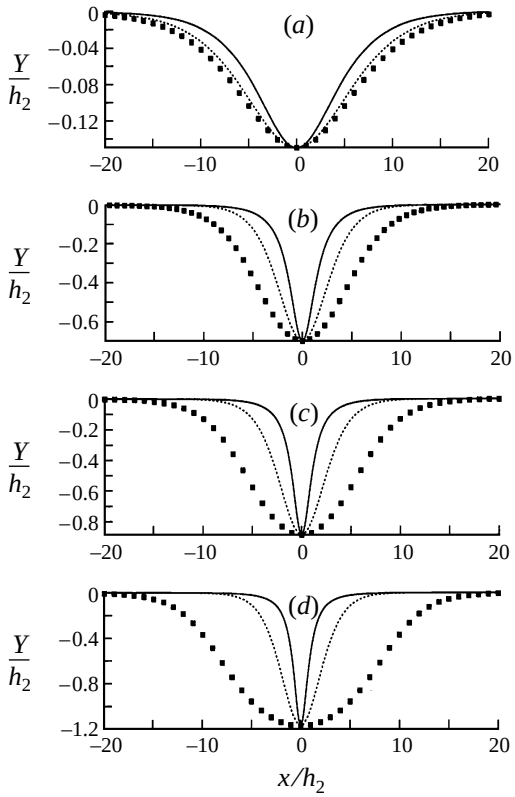

FIGURE 4. Profiles of solitary waves obtained by fully nonlinear (filled squares), KdV (dotted line) and finite-depth (solid line) theories. $h_1/h_2 = 4$ and $t = 0$ in all cases. (*a*) $|Y|_{max}/h_2 = 0.15$, $\mu = 0.9$; (*b*) $|Y|_{max}/h_2 = 0.7$, $\mu = 0.9$; (*c*) $|Y|_{max}/h_2 = 0.888$, $\mu = 0.8114$; (*d*) $|Y|_{max}/h_2 = 1.171$, $\mu = 0.8114$. (Note the differences in vertical scale.)

in an early phase; however, preliminary results show very good comparison with the strongly nonlinear interface method, even for a not very sharp pycnocline.

Figure 4 again illustrates that the sech^2-profiles from the KdV theory are closer to the fully nonlinear solution than those due to the finite-depth theory, in spite of the relatively large ratio between h_1 and h_2 in these examples which might lead us to believe that the opposite should be true. This somewhat surprising result has been explained by Segur & Hammack (1982) who found that the range of validity of the finite-depth theory with regard to nonlinearity is far more limited than that for the KdV theory, so that the former theory produce unrealistic results much earlier than the latter.

5. Transcritical flow over topography

We now apply the model to transcritical two-layer flow over a bottom topography. There are several questions concerning this subject: Under which conditions is the flow unsteady? Another aspect is upstream influence in stratified flows, which in part can be addressed by the present two-layer model. Furthermore, for which conditions may transcritical flow over topography generate upstream solitary waves? These topics have been discussed in earlier works describing observations in nature, laboratory experiments and theoretical models. The theoretical models used are

basically from hydraulic nonlinear theory, see e.g. Baines (1984), Grimshaw & Smyth (1986), or weakly nonlinear dispersive models, see e.g. Miles (1979, 1981), Melville & Helfrich (1987), Zhu *et al.* (1987). These methods have limited validity with regard to nonlinearity and dispersion, however, and give unrealistic predictions for finite-amplitude and moderate wavelength.

Melville & Helfrich (1987, referred to below as MH), described two sets of experiments on interfacial transcritical flow over topography. They compared the experiments with simulations using the forced KdV equation and an extended KdV model, where in the latter a cubic nonlinearity was taken into account in addition to the usual quadratic nonlinearity. They got, however, a poor agreement between theory and experiments when the ratio between the depths of the layers was 1 to 4, but better agreement when the ratio was 1 to 2. We shall apply our method to the set of experiments of MH where the disagreements between the KdV models and the observations were most severe, and we shall find a very good agreement between the fully nonlinear model and the experiments. Furthermore, we shall apply our model to investigate generation of upstream solitary waves in transcritical flows.

The data for the set of experiments of MH we shall compare with are as follows: $\rho_2 = 0.8$ g cm^{-3}, $h_2 = 3$ cm, $\rho_1 = 0.986$ g cm^{-3}, $h_1 = 12$ cm. The effect of a bottom topography was simulated in the experiments by moving a body in the upper layer with a profile given by $y = h_2 - H_0\mathrm{sech}^2(Kx)$, where $KH_0 = 0.1989$ (this geometry is the two-dimensional counter-part of Nansen's ship). The height of the body was determined by $H_0/h_0 = 0.5$, with the reference depth $h_0 = h_1h_2/(h_1 + h_2)$. (This means that $H_0/h_2 = 0.4$.) MH used a tank of length $L = 15$ m ($L/h_2 = 500$) and recorded the displacement of the interface after 5 m ($x_1/h_2 = 166$), hereafter referred to as station 1, and the horizontal velocity in the lower layer after 9.25 m ($x_2/h_2 = 308$), hereafter referred to as station 2. At the latter station photographs of the interface were also taken. (We note that MH, p. 36 give $H_0 = 5.1$ cm, which, however, does not seem to fit with the other data given.)

We use all the above conditions in our simulations, except at the upper boundary, where the free surface is replaced by a rigid wall.

5.1. *Speed and elevation of the upstream disturbance*

As reference speed we shall use the linear shallow water speed c_0 given by (47). In MH (equation (2.6) and p. 34), applying the Boussinesq approximation, their reference speed is given by $\tilde{c}_0 = [gh_0(\rho_1 - \rho_2)/\rho_0]^{1/2}$, where ρ_0, however, is not explicitly defined. It seems likely that ρ_0 would be chosen equal to ρ_1, and we have used this reference density in the comparisons. This gives a very good agreement between their experiments and our comparisons, see figure 5. If ρ_0 is chosen such that $\tilde{c}_0 = c_0$ we still get a fair agreement.

In the first comparison we consider the speed c of the leading disturbance of the interface as a function of the speed U of the geometry. This is one of the most robust quantities to measure and compare, and was determined in the experiments by recording the elapsed time of the leading disturbance between the recording stations. We have followed the same procedure in extracting c from the computations, and the excellent agreement is shown in figure 5(a).

Next we show in figure 5(b) the maximum elevation $|Y|_{max}$ of the upstream disturbance. We use the same vertical scale as MH (with h_0 as vertical reference length). The computations show that $|Y|_{max}$ is growing somewhat as the body moves down the wave-tank, and we therefore present results when the waves have reached the far end of the tank. The agreement between the model and the experiments is in

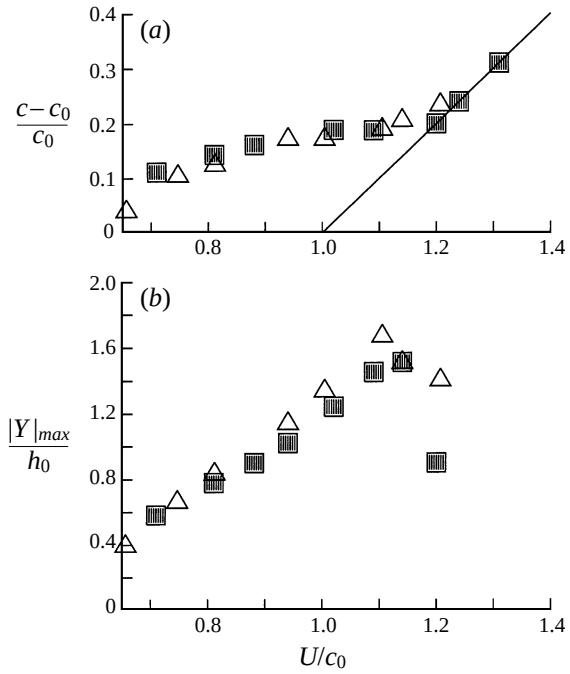

FIGURE 5. (*a*) Excess speed $(c-c_0)/c_0$ and (*b*) maximum elevation of leading upstream disturbance vs. U/c_0. Filled squares: present theory. Triangles: experiments by Melville & Helfrich, figure 11. Solid line in (*a*) marks solution moving with the same speed as the body.

general very good, but we note that the model somewhat underpredicts the measured elevations when the speed of the body exceeds c_0. For Froude number $U/c_0 = 1.2$ we compute a significantly smaller value for $|Y|_{max}$ than measured. We are not sure about the reason for this disagreement, but we note that this Froude number is close to the upper limit of the transcritical domain in this example, where the maximal elevation as function of the Froude number drops significantly.

MH noted that the curves for $(c-c_0)/c_0$ and $|Y|_{max}/h_0$ in figure 5 with the scaling shown should coincide, according to KdV theory. These curves have, however, quite different forms. Our computations confirm the experimental observations.

5.2. *Profiles of the interface*

We next consider simulations of the interface elevation and compare with reproduced recordings from MH, figure 10. In the experiments the elevation $Y(t;x_1)$ at station 1 and the horizontal velocity $u_1(t;x_2)$ in the lower layer at station 2 are recorded. All recordings are functions of time. The computed interface profiles $Y(x, t = \text{const.})$ are shown for time instants when the body is (approximately) at station 1 (solid line) and at station 2 (dashed line). The body started at $x = 0$. (We use the same vertical scale as MH.)

In figures 6–8 are shown comparisons for three different choices of U: $U/c_0 = 0.81$ $(U/\tilde{c}_0 = 0.88)$, $U/c_0 = 0.94$ $(U/\tilde{c}_0 = 1.02)$, $U/c_0 = 1.14$ $(U/\tilde{c}_0 = 1.24)$. In the cases when $U/c_0 < 1$, figures 6 and 7, both theory and experiments show that an upstream undular depression is generated, with a number of local crests which is increasing with time. The elevation behind the body reaches a maximum level at about 40% of the thickness of the upper layer, and is continuously growing horizontally with

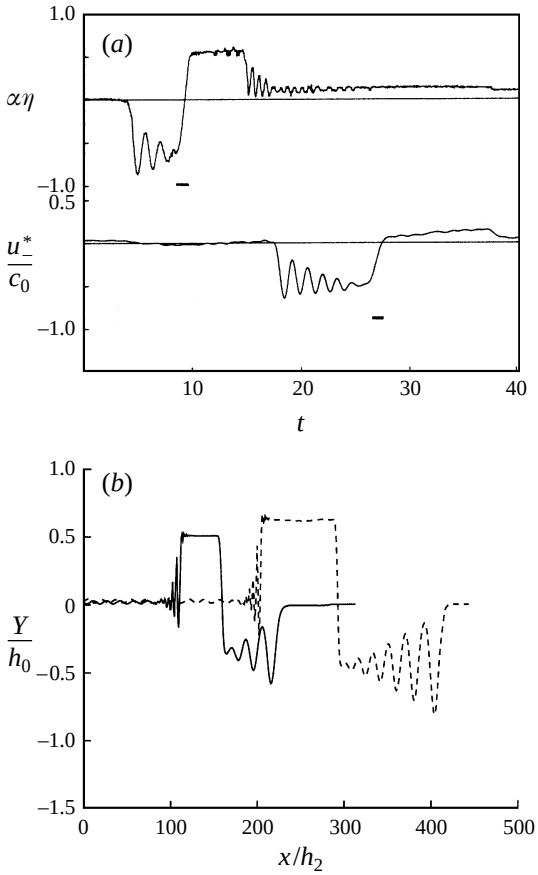

FIGURE 6. Elevation of interface. $U/c_0 = 0.81$. (*a*) Experimental recordings reproduced from MH figure 10(*a*) ($U/\tilde{c}_0 = 0.881$). (*b*) Present method, same vertical scale as in the experiments ($h_0 = 0.8h_2$). $t(g/h_2)^{1/2} = 480$ (solid line), $t(g/h_2)^{1/2} = 870$ (dashed line). $\mu = 0.8114$, $h_1/h_2 = 4$, $\Delta t(g/h_2)^{1/2} = 0.5$, $\Delta T(g/h_2)^{1/2} = 5$ (smoothing interval), $\Delta x/h_2 = 1$, $N = 501$, $N_B = 80$, $\alpha = 1$. (Computations with $\Delta t(g/h_2)^{1/2} = 1$ give the same results.)

time. For $U/c_0 = 1.14$ (figure 8) theory and experiment show that a depression of appreciable magnitude is generated close to the body, with speed slightly larger than U. The flow is clearly unsteady, as an elevation downstream and a corresponding volume upstream is continuously developing. The upstream depression becomes a solitary wave after sufficiently large time.

All computations reproduce the experiments with striking agreement. The number of local wave crests of the upstream disturbance which pass the recording stations, and the elevation behind the body are almost exactly reproduced by the theory. We have run convergence checks confirming the computations shown. We have no explanation for why the theoretical depression is systematically somewhat smaller than the recordings, but we speculate that the deviation between the computations and the measurements falls within the error bounds of the interface recorder used in the experiments.

In figure 7(*a*) are also shown simulations by MH using the KdV equation, which exhibit twice as many peaks of the upstream undular depression as the observations in the wave tank and the fully nonlinear computations.

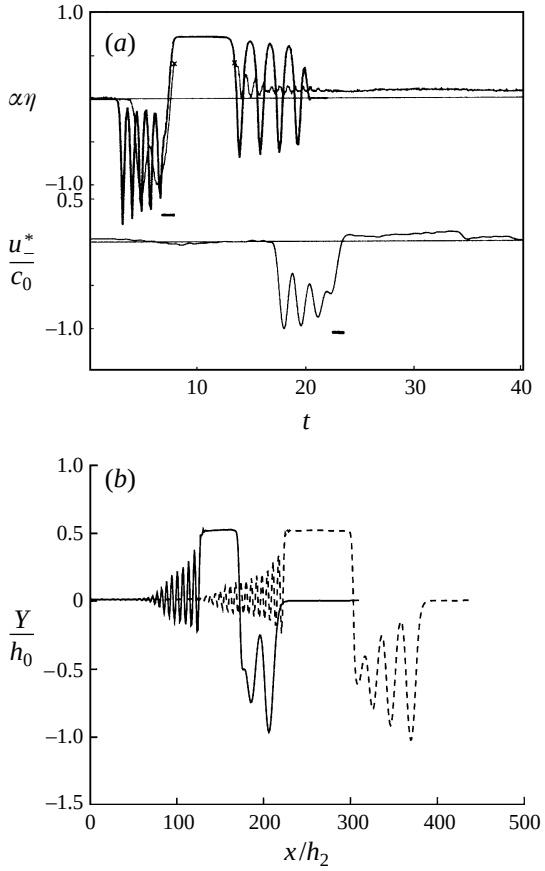

FIGURE 7. Same as figure 6 but $U/c_0 = 0.94$. (*a*) MH figure 10(*b*) ($U/\tilde{c}_0 = 1.02$); heavy solid line: solution by the forced KdV equation. (*b*) Present method. $t(g/h_2)^{1/2} = 450$ (solid line), $t(g/h_2)^{1/2} = 780$ (dashed line).

The simulations in figures 5–8 were performed with $\Delta t(g/h_2)^{1/2} = 0.5$ and 1, giving the same results. Convergence of the transient simulations are further documented by the comparisons in figures 10 and 11 below.

5.3. *Regime of unsteady transcritical flow*

We find that the flow is unsteady for $0.38 \lesssim U/c_0 \lesssim 1.2$. In this regime the simulations show that the fluid volume upstream, being an undular depression or a train of solitary waves (see §5.4), and the length of the elevation behind the body are steadily increasing with time. When $U/c_0 > 1.2$, supercritical flow is obtained. The transient waves due to the startup of the body are then swept downstream and a steady state is reached. When $U/c_0 < 0.4$, a train of steady lee waves is generated behind the body. Analytical estimates of the unsteady regime of transcritical flow are derived by means of asymptotic theories for free surface flows by Miles (1986), and for interfacial waves by MH. The latter estimate predicts in the present example a lower limit which is quite unrealistic and a range of transcritical flow that is too wide.

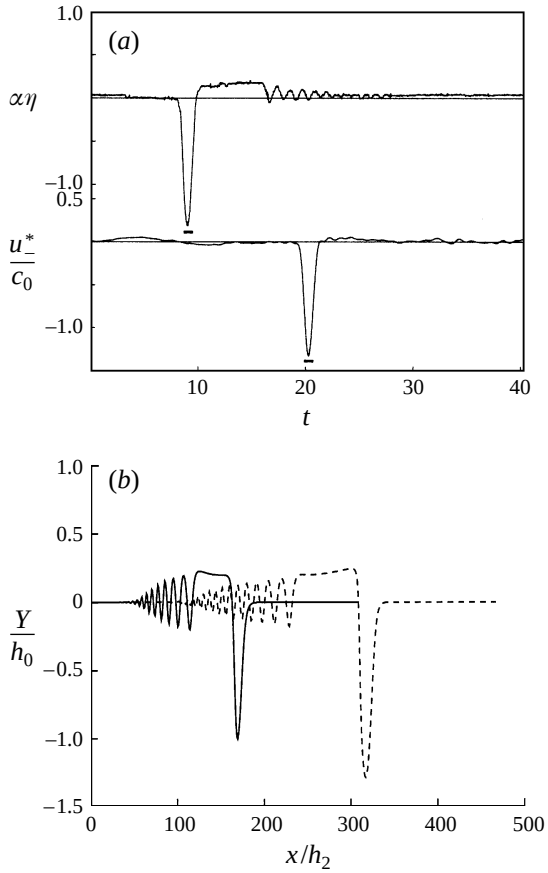

FIGURE 8. Same as figure 6 but $U/c_0 = 1.14$. (*a*) MH figure 10c ($U/\tilde{c}_0 = 1.24$). (*b*) Present method. $t(g/h_2)^{1/2} = 360$ (solid line), $t(g/h_2)^{1/2} = 660$ (dashed line).

5.4. *Upstream solitary waves*

When the speed of the body is in the transcritical regime, but less than c_0, an undular upstream depression is generated. This is also true when U slightly exceeds c_0. (We have performed simulations for $U/c_0 = 1.02$, finding an upstream undular depression in this case.) In the remaining part of the transcritical regime we find that solitary waves propagating upstream are generated by the body. Computations are performed for U/c_0=1.09, 1.1, 1.14. In order to investigate the last regime more closely we first fix the speed to $U/c_0 = 1.09$ and vary the height of the body from a small to a large value. More precisely, we let the body be determined by $y = h_2 - \tilde{H}_0\mathrm{sech}^2(Kx)$, where $\tilde{H}_0$ takes the values $\tilde{H}_0 = 0.125H_0$, $0.25H_0$, $0.5H_0$, H_0. Here, $H_0 = 0.4h_2$ as before, which means that the body, for $\tilde{H}_0 = H_0$, is the same as that in the examples shown in figures 5–8. Increasing the value of $\tilde{H}_0$ gives a larger forcing of the flow, but it also corresponds to imposing stronger nonlinearity on the problem. We show in figure 9 the resulting profiles of the interface after non-dimensional times $t(g/h_2)^{1/2} = 1020$, 1500, when the body is at $x/h_2 = 469$, 689, respectively. The maximal depressions in the figure correspond to those of the solitary waves shown in figure 4.

In the first case the flow is developing towards supercritical flow, practically speaking, and the depression at the position of the body is rather small. When we increase

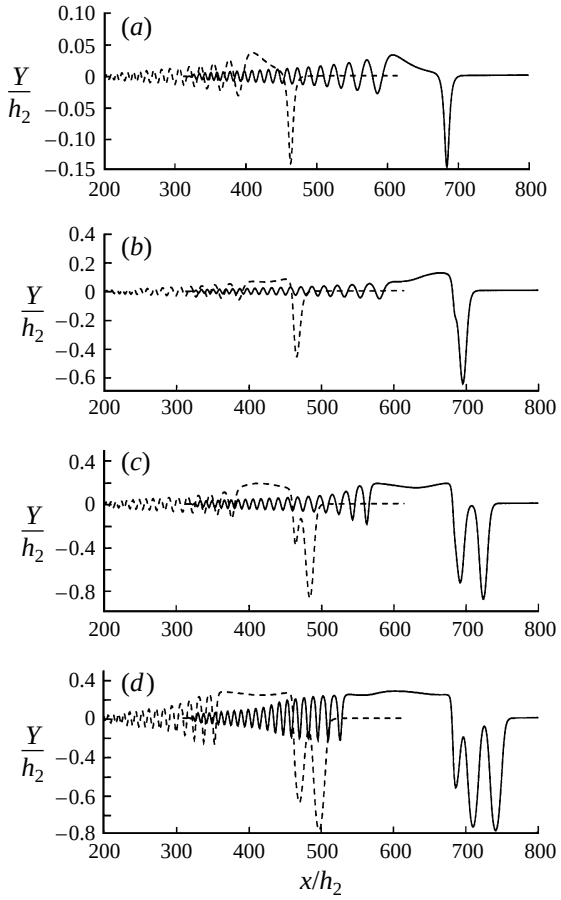

FIGURE 9. Elevation of interface. $Fr = 1.09$. Increasing height $\tilde{H}_0$ of moving body, i.e. geometry $\tilde{H}_0 \mathrm{sech}^2 Kx$. $t(g/h_2)^{1/2} = 1020$ (dashed line), $t(g/h_2)^{1/2} = 1500$ (solid line). (*a*) $\tilde{H}_0 = 0.125H_0$, (*b*) $\tilde{H}_0 = 0.25H_0$, (*c*) $\tilde{H}_0 = 0.5H_0$, (*d*) $\tilde{H}_0 = H_0$. $\mu = 0.8114$, $h_1/h_2 = 4$, $\Delta t(g/h_2)^{1/2} = 0.5$, $\Delta T(g/h_2)^{1/2} = 5$ (smoothing interval), $\Delta x/h_2 = 1$, $N = 501$, $N_B = 80$, $\alpha = 1$. (Note the differences in vertical scale.)

$\tilde{H}_0$ from $0.125H_0$ to $0.25H_0$ the change is rather large. Now the flow has become unsteady, an elevation behind the body is continuously developing, and the depression slightly ahead of the body attains a rather large peak which slowly develops into a solitary wave. The next two examples show the initial phases of generation of upstream solitary waves. We observe in the last case (figure 9*d*) that one solitary wave already been generated before the geometry has passed the location $x/h_2 = 500$, corresponding to the length of the wave tank used in the experiments by MH. This means that solitary waves should, according to the simulations, have been observed in their laboratory experiments for this depth ratio if they had taken relevant measurements at the end of the wave tank.

In order to more closely examine the properties of the simulated upstream waves we compare with steady solitary wave solutions obtained by solving the equations with the body absent, in a frame of reference following one wave, given the value of $|Y|_{max}/h_2$. The comparisons are displayed in figure 10(*a*, *b*) and show that the time simulations have produced leading waves having exactly the same forms as the steadily progressing solutions. In the first case ($\tilde{H}_0 = 0.5H_0$) the amplitude is $|Y|_{max}/h_2 = 0.888$, and we

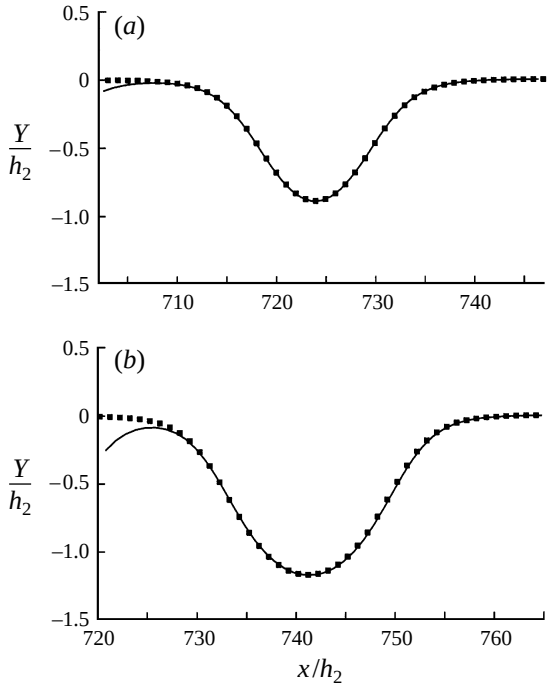

FIGURE 10. Comparison between simulated leading upstream wave (solid line) and solitary wave solution, steady profile (filled squares). (*a*) Same as figure 9*c* (body geometry given by $0.5H_0\mathrm{sech}^2Kx$). $|Y|_{max}/h_2 = 0.888$. (*b*) Same as figure 9*d* (geometry given by $H_0\mathrm{sech}^2Kx$). $|Y|_{max}/h_2 = 1.171$.

find that the propagation velocity in the time simulation is $c_{sim}/(gh_2)^{1/2} = 0.5007$, while the solution of the steady equations gives $c_{steady}/(gh_2)^{1/2} = 0.5008$. In the other case ($\tilde{H}_0 = H_0$) the corresponding results are $|Y|_{max}/h_2 = 1.171$, $c_{sim}/(gh_2)^{1/2} = 0.5091$ and $c_{steady}/(gh_2)^{1/2} = 0.5092$. For comparison, $c_0/(gh_2)^{1/2} = 0.4215$. This very good agreement documents that the leading upstream waves indeed may be termed solitary waves.

The transcritical simulations in figure 9 show mainly that upstream solitary waves with non-dimensional amplitude of order unity are generated when the height of the topography is moderate, which means that a rather pronounced upstream effect takes place. The upstream waves disappear, however, when the topography becomes too small.

Finally we consider a different example with a thick layer above a thin, where $\mu = 0.7873$ and $h_2/h_1 = 4$. The non-dimensional linear shallow water speed c_0 is the same as in figures 9 and 10. A half-elliptical bottom topography with horizontal half-axis $10h_1$ and vertical half-axis $0.1h_1$ is moving with speed $U/c_0 = 1.1$ in the lower layer. This topography has approximately the same volume as the previous one, but imposes weaker nonlinearity on the problem, since the height of the topography now is only 10% of the thinner layer. We have performed a very long time simulation with this configuration (5520 time steps), and show the results in figure 11. At non-dimensional time $t(g/h_1)^{1/2} = 1080$ two solitary waves are generated, at $t(g/h_1)^{1/2} = 1920$ almost four, and at $t(g/h_1)^{1/2} = 2760$ almost six. The depression behind the topography stabilizes at a level of 80% of the initial thickness of the lower fluid.

The solitary waves all have the same amplitude, within a variation of 0.3%. Upon

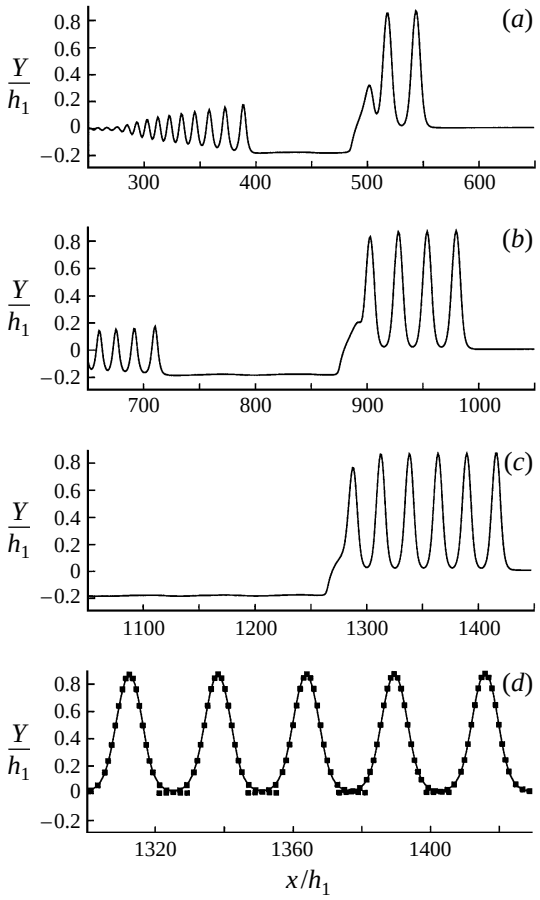

FIGURE 11. Generation of upstream solitary waves. Moving bottom topography is a half-ellipse, horizontal half-axis $10h_1$, vertical half-axis $0.1h_1$. $U/c_0 = 1.1$, $\mu = 0.7873$, $h_2/h_1 = 4$. (*a*) $t(g/h_1)^{1/2} = 1080$, (*b*) $t(g/h_1)^{1/2} = 1920$, (*c*) $t(g/h_1)^{1/2} = 2760$, (*d*) Close up of (*c*), filled squares mark steady solitary wave solution with $|Y|_{max}/h_1 = 0.869$. $\Delta t(g/h_1)^{1/2} = 0.5$, $\Delta T(g/h_1)^{1/2} = 3$ (smoothing interval), $\Delta x/h_1 = 1$, $N = 501$, $N_B = 80$, $\alpha = 0$.

comparing with the solution of a steady profile with $|Y|_{max}/h_1 = 0.869$, we find a striking agreement between the computed profiles, see figure 11(*d*), and the wave speed: $c_{sim}/(gh_1)^{1/2} = 0.5192$, $c_{steady}/(gh_1)^{1/2} = 0.5191$. Thus, the simulated waves may be regarded as a train of solitary waves. The comparison documents the high accuracy of the time simulations.

We find that the distance between the peaks is almost the same, except for a small oscillation of order less than 1% of a mean value of about $28.5h_1$, which indicates that a weak interaction is taking place between the individual waves. For $t(g/h_1)^{1/2} = 2760$, the distance between the leading and the second wave is somewhat larger.

We have also performed simulations with an ellipse with half-axes $0.05h_1$ and $10h_1$, moving at $U/c_0 = 1.1$. In this case also solitary waves are generated, with $|Y|_{max}/h_1 = 0.7006$ and $c_{sim}/(gh_1)^{1/2} = 0.5068$, i.e. a rather pronounced upstream influence.

More data from the simulations, for four different cases A–D, are summarized in table 3. The data show that, for fixed volume, a taller body generates solitary

	A_{body}	U/c_0	c_w	$\lvert Y\rvert_{max}$	A_w	Δx peak-peak	$(c_w - U)/\Delta x$
A	$0.81\,h_2^2$	1.09	$0.5007\,(gh_2)^{1/2}$	$0.888\,h_2$	$11.74\,h_2^2$	—	—
B	$1.61\,h_2^2$	1.09	$0.5091\,(gh_2)^{1/2}$	$1.171\,h_2$	$19.79\,h_2^2$	$31.3\,h_2$	$0.00159\,(g/h_2)^{1/2}$
C	$(\pi/4)\,h_1^2$	1.1	$0.5068\,(gh_1)^{1/2}$	$0.701\,h_1$	$6.59\,h_1^2$	—	—
D	$(\pi/2)\,h_1^2$	1.1	$0.5192\,(gh_1)^{1/2}$	$0.869\,h_1$	$8.33\,h_1^2$	$28.5\,h_1$	$0.00195\,(g/h_1)^{1/2}$

TABLE 3. Upstream generation of solitary waves. Case A: figure 9(*c*) ($\tilde{H}_0 = 0.5H_0$) $\mu = 0.8114$ and $h_1/h_2 = 4$. Case B: figure 9(*d*) ($\tilde{H}_0 = H_0$) $\mu = 0.8114$ and $h_1/h_2 = 4$. Case C: ellipse with half-axes $10h_1$, $0.05h_1$, $\mu = 0.7873$ and $h_2/h_1 = 4$. Case D: figure 11, ellipse with half-axes $10h_1$, $0.1h_1$, $\mu = 0.7873$ and $h_2/h_1 = 4$. A_{body}: cross-section area of body; c_w: solitary wave speed; A_w: cross-section area over/under one solitary wave; Δx: distance between wave peaks. (Non-dimensional c_0 is the same in all cases.)

waves with higher amplitude, larger volume and a somewhat longer peak-to-peak distance, than a shorter body. We find, on the other hand, that the wave speed relative to the speed of the body, $c_w - U$, becomes smaller in cases A and B than in C and D. The generation rate of solitary waves, determined by $(c_w - U)/$(peak-to-peak distance), becomes somewhat higher for the example in figure 11 than in figure 9(*d*).

6. Conclusion

We have described a fully nonlinear time-stepping method for unsteady motion of a two-layer fluid. Essential parts of the method are the use of Taylor series expansions of the prognostic equations, application of spatial finite difference formulae of high order and application of Cauchy's theorem to solve the Laplace equation. The latter is found to be superior to other methods with regard to avoiding instability, a result which is partly explained by a stability analysis showing that the scheme is neutrally stable for linear flows. Details of the numerical implementation are described and convergence of the method is documented in several examples. The spatial step length, Δx, must be less than twice the smallest thickness of the thinner layer, in order to maintain analyticity of the function representing the image of the interface, see (20). In most of the computations Δx is set equal to the thickness of the thinner layer. We may use a relatively large time step and still achieve a high accuracy of the computations. The method is computationally very efficient and is suitable for long time simulations. The velocity profiles in the fluids are inherent to the formulation and may easily be extracted from the computations (we have not shown velocity profiles here).

Fully nonlinear solitary wave profiles are compared with available experiments, finding very good agreement. Upon comparing with weakly nonlinear theories (KdV, BO and finite-depth) we find that these theories have quite limited ranges of validity, and that they predict unrealistic wave shapes when the maximum elevation becomes comparable to the thickness of the thinner layer.

We apply the model to simulate a set of experiments by Melville & Helfrich (1987) on unsteady transcritical flow at a moving body, where KdV theory was reported to give unrealistic results. We find here a satisfactory agreement between the fully nonlinear theory and the experiments. Furthermore, the unsteady transcritical regime is identified, where an undular depression is generated when the speed of the geometry is less than a value which somewhat exceeds the critical speed, and a train of solitary

waves is generated otherwise. A corresponding elevation of constant level develops behind the geometry. Then the generation of upstream solitary waves by a moving body is investigated in detail for some examples, finding that trains of solitary waves with appreciable heights are propagating upstream. We have compared the simulated waves with solitary wave profiles obtained by solving the nonlinear equations in a frame of reference following the waves, where the propagation speed is determined from the equations. There is a very good agreement between the simulated and steady profiles. Even the propagation speed is reproduced in the time simulations with a relative accuracy of 0.02%.

In the examples discussed in §5 the ratio between the depths of the layers is 1 to 4. In all examples we find that a moving body generates upstream disturbances with rather large depression (elevation). We have performed simulations for other bodies with smaller heights, imposing a correspondingly weaker nonlinearity to the problem. Still we find that waves with rather large amplitudes are generated (the volume of the body cannot be too small). Upon comparing with the results in §4 we find that the flow is clearly outside the ranges of validity of the KdV and finite-depth theories. We find that the same conclusion applies to the BO theory (results not shown here). Our results thus indicate that weakly nonlinear theories have quite limited applications in modelling unsteady transcritical two-layer flows when $h_1/h_2 \gg 1$ (or $h_2/h_1 \gg 1$), and that a fully nonlinear method in general is required for this purpose. There may be exceptions for very long bodies with very small height.

The remarkable discrepancies between the weakly nonlinear theories and the present fully nonlinear interface method motivated us to set up experiments on internal waves at the University of Oslo. The experiments are in an early phase, however, preliminary results show very good comparison with the present method, even for not very sharp pycnocline.

The method may be used to investigate collision properties of steep interfacial solitary waves, and their interaction with a fixed geometry in the ocean or a bottom topography (work is in progress). Furthermore, we may use the method to simulate tidal generated interfacial waves at a sill, and the transient development of a large hump into solitary waves.

At the free surface we have used the rigid lid approximation. The method may, however, be generalized to model the motion of the free surface also.

This research was supported by The Research Council of Norway through Research Fellowships for H.A.F and P.O.R. and a grant of computing time (Programme for Supercomputing).

Appendix A. Pseudo-Lagrangian derivatives at the interface

To derive integral equations for $\partial\phi_{1v}/\partial t$, $\partial\Upsilon_\xi/\partial t$, $\partial^2\phi_{1v}/\partial t^2$ and $\partial^2\Upsilon_\xi/\partial t^2$, pseudo-Lagrangian derivatives of the kinematic boundary condition at the interface are required. Taking the pseudo-Lagrangian derivative of (2) we find

$$\frac{\mathrm{D}_\times}{\mathrm{d}t}(\boldsymbol{v}_1\cdot\hat{\boldsymbol{n}}-\boldsymbol{v}_2\cdot\hat{\boldsymbol{n}})=\hat{\boldsymbol{n}}\cdot\frac{\mathrm{D}_\times}{\mathrm{d}t}(\boldsymbol{v}_1-\boldsymbol{v}_2)+(\boldsymbol{v}_1-\boldsymbol{v}_2)\cdot\frac{\mathrm{D}_\times\hat{\boldsymbol{n}}}{\mathrm{d}t}=0 \tag{A 1}$$

where a scaled normal vector $\hat{\boldsymbol{n}}=|z_\xi|\boldsymbol{n}=(-Y_\xi,X_\xi)$ at I is introduced for convenience.

Noting that

$$\frac{\mathrm{D}_\times \hat{\boldsymbol{n}}}{\mathrm{d}t} = \frac{\partial}{\partial t}(-Y_\xi(\xi,t), X_\xi(\xi,t)) = \frac{\partial}{\partial \xi}(-Y_t(\xi,t), X_t(\xi,t)) = (-v_{\times\xi}, u_{\times\xi}) \tag{A 2}$$

equation (A 1) gives

$$\begin{aligned}\frac{\partial \phi_{1v}}{\partial t} - \frac{\partial \phi_{2v}}{\partial t} = {} & y_\xi[u_\times(u_{1x}-u_{2x}) + v_\times(v_{1x}-v_{2x})] \\ & -x_\xi[u_\times(v_{1x}-v_{2x}) + v_\times(-u_{1x}+u_{2x})] + (u_1-u_2)v_{\times\xi} + (v_1-v_2)u_{\times\xi}\end{aligned} \tag{A 3}$$

which is used to derive integral equations for $\partial\phi_{1v}/\partial t$, $\partial Y_\xi/\partial t$, similar to (28)–(29).

Next we consider

$$\frac{\mathrm{D}_\times^2}{\mathrm{d}t^2}(\boldsymbol{v}_1\cdot\boldsymbol{n} - \boldsymbol{v}_2\cdot\boldsymbol{n}) = 0. \tag{A 4}$$

By carrying out the differentiation we obtain

$$\begin{aligned}\frac{\partial^2\phi_{1v}}{\partial t^2} - \frac{\partial^2\phi_{2v}}{\partial t^2} = {} & -\hat{\boldsymbol{n}}\cdot\{\boldsymbol{v}_\times\cdot\nabla\left(\frac{\partial \boldsymbol{v}_1}{\partial t} - \frac{\partial \boldsymbol{v}_2}{\partial t}\right) + \frac{\partial}{\partial t}[\boldsymbol{v}_\times\cdot\nabla(\boldsymbol{v}_1-\boldsymbol{v}_2)] \\ & -\boldsymbol{v}_\times\cdot\nabla[\boldsymbol{v}_\times\cdot\nabla(\boldsymbol{v}_1-\boldsymbol{v}_2)]\} + 2\frac{\mathrm{D}_\times\hat{\boldsymbol{n}}}{\mathrm{d}t}\cdot\frac{\mathrm{D}_\times}{\mathrm{d}t}(\boldsymbol{v}_1-\boldsymbol{v}_2) - (\boldsymbol{v}_1-\boldsymbol{v}_2)\cdot\frac{\mathrm{D}_\times^2\hat{\boldsymbol{n}}}{\mathrm{d}t^2}\end{aligned} \tag{A 5}$$

where $\mathrm{D}_\times\hat{\boldsymbol{n}}/\mathrm{d}t$ is determined by (A 2) and

$$\frac{\mathrm{D}_\times^2\hat{\boldsymbol{n}}}{\mathrm{d}t^2} = \left(-\left(\frac{\mathrm{D}_\times v_\times}{\mathrm{d}t}\right)_\xi, \left(\frac{\mathrm{D}_\times u_\times}{dt}\right)_\xi\right) \tag{A 6}$$

Equation (A 5) is used to derive integral equations for $\partial^2\phi_{1v}/\partial t^2$, $\partial^2 Y_\xi/\partial t^2$, similar to (28)–(29).

Pseudo-derivatives of ψ are found by differentiating the dynamical boundary condition at the interface.

Appendix B. The integral equations in discrete form

The discrete forms of the integral equations (28), (29) and (30) are given by

$$\begin{aligned}\pi Y_\xi(\xi') = {} & \frac{2}{\mu+1}\sum_{\xi=1}^{N}\mathscr{B}(\xi',\xi)\psi_\xi(\xi) + \frac{\mu-1}{\mu+1}\sum_{\xi=1}^{N}\mathscr{B}(\xi',\xi)Y_\xi(\xi) \\ & + \sum_{\xi=1}^{N}[\mathscr{A}_1(\xi',\xi) - \mathscr{A}_2(\xi',\xi)]\phi_{1v}(\xi) + \frac{1}{1+\mu}\sum_{\xi=1}^{N}[-\mathscr{B}_1(\xi',\xi) - \mathscr{B}_2(\xi',\xi)]\psi_\xi(\xi) \\ & + \frac{1}{1+\mu}\sum_{\xi=1}^{N}[-\mu\mathscr{B}_1(\xi',\xi) + \mathscr{B}_2(\xi',\xi)]Y_\xi(\xi) + \sum_{\xi=1}^{N_B}[-\mathscr{A}(\xi',\xi) + \mathscr{A}_1(\xi',\xi)]\phi_{1v}(\xi) \\ & + \sum_{\xi=1}^{N_B}[\mathscr{B}(\xi',\xi) - \mathscr{B}_1(\xi',\xi)]\phi_{1\xi}(\xi) \qquad (z' \text{ on } I),\end{aligned} \tag{B 1}$$

$$\pi(1+\mu)\phi_{1v}(\xi') = \sum_{\xi=1}^{N} \mathscr{A}(\xi',\xi)\psi_{\xi}(\xi) - \psi_{\xi\xi}(\xi') + (1-\mu)\sum_{\xi=1}^{N} \mathscr{B}(\xi',\xi)\phi_{1v}(\xi)$$
$$+\frac{1}{1+\mu}\sum_{\xi=1}^{N}[\mathscr{A}_1(\xi',\xi)+\mu\mathscr{A}_2(\xi',\xi)]\psi_{\xi}(\xi)$$
$$+\frac{\mu}{1+\mu}\sum_{\xi=1}^{N}[\mathscr{A}_1(\xi',\xi)-\mathscr{A}_2(\xi',\xi)]\Upsilon_{\xi}(\xi)$$
$$-\sum_{\xi=1}^{N}[-\mathscr{B}_1(\xi',\xi)+\mu\mathscr{B}_2(\xi',\xi)]\phi_{1v}(\xi)+\sum_{\xi=1}^{N_B}[\mathscr{A}(\xi',\xi)+\mathscr{A}_1(\xi',\xi)]\phi_{1\xi}(\xi)$$
$$+\sum_{\xi=1}^{N_B}[\mathscr{B}(\xi',\xi)+\mathscr{B}_1(\xi',\xi)]\phi_{1v}(\xi) \qquad (z' \text{ on } I), \tag{B 2}$$

$$\pi\phi_{1\xi}(\xi') = \sum_{\xi=1}^{N}[-\mathscr{A}(\xi',\xi)+\mathscr{A}_1(\xi',\xi)]\phi_{1v}(\xi) + \frac{1}{1+\mu}\sum_{\xi=1}^{N}[\mathscr{B}(\xi',\xi)-\mathscr{B}_1(\xi',\xi)]\psi_{\xi}(\xi)$$
$$+\frac{\mu}{1+\mu}\sum_{\xi=1}^{N}[\mathscr{B}(\xi',\xi)-\mathscr{B}_1(\xi',\xi)]\Upsilon_{\xi}(\xi)$$
$$+\sum_{\xi=1}^{N_B}[-\mathscr{A}(\xi',\xi)+\mathscr{A}_1(\xi',\xi)]\phi_{1v}(\xi)+\phi_{1v\xi}(\xi')$$
$$+\sum_{\xi=1}^{N_B}[\mathscr{B}(\xi',\xi)-\mathscr{B}_1(\xi',\xi)]\phi_{1\xi}(\xi), \qquad (z' \text{ on } B) \tag{B 3}$$

where $\mathscr{A}+\mathrm{i}\mathscr{B}$ is given by (35) and $\mathscr{A}_j+\mathrm{i}\mathscr{B}_j$ $(j=1,2)$ by

$$\mathscr{A}_j+\mathrm{i}\mathscr{B}_j = \left(\frac{z'_{\xi}}{z^*-z'+(-1)^j 2\mathrm{i}h_j}\right)^*, \qquad j=1,2 \tag{B 4}$$

REFERENCES

Amick, C. J. & Turner, R. E. L. 1986 A global theory of internal solitary waves in two-fluid systems. *Trans. Am. Math. Soc.* **298**, 431.

Apel, J. R., Holbrook, J. R., Liu, A. K. & Tsai, J. 1985 The Sulu Sea internal soliton experiment. *J. Phys. Oceanogr.* **15**, 1625.

Baines, P. 1984 A unified description of two-layer flow over topography. *J. Fluid Mech.* **146**, 127.

Baker, G. R., Meiron, D. I. & Orszag, S. A. 1982 Generalized vortex methods for free-surface flow problems. *J. Fluid Mech.* **123**, 477.

Benjamin, T. B. 1967 Internal waves of permanent form in fluids of great depth. *J. Fluid Mech.* **29**, 559.

Casciola, C. M. & Landrini, M. 1996 Nonlinear long waves generated by a moving pressure disturbance. *J. Fluid Mech.* **325**, 399.

Davis, R. E. & Acrivos, A. 1967 Solitary internal waves in deep water. *J. Fluid Mech.* **29**, 593.

Dold, J. W. 1992 An efficient surface-integral algorithm applied to unsteady gravity waves *J. Comput. Phys.* **103**, 90.

Dold, J. W. & Peregrine, D. H. 1985 An efficient boundary-integral equation method for steep unsteady water waves. In *Numerical Methods for Fluid Dynamics*, vol. 2 (ed. K. W. Morton & M. J. Baines), Clarenden, pp. 671–679.

Eliassen, A. 1982 Vilhelm Bjerknes and his students. *Ann. Rev. Fluid Mech.* **14**, 1.

Eliassen, A. & Fjørtoft, R. 1992 The interface method for calculating the temporal evolution of a two-fluid system. *Frontiers of Science, Ann. NY Acad. Sci.* **661**, 54.

Farmer, D. M. & Smith, J. D. 1980 Tidal interaction of stratified flow with a sill in Knight Inlet. *Deep-Sea Res.* **27A**, 239.

Friis, H. A. 1995 On nonlinear free surface and interfacial water waves and their interaction with submerged bodies. Dr. Scient. Thesis, Dept. of Mathematics, The University of Oslo.

Grimshaw, R. H. J. & Smyth, N. 1986 Resonant flow of a stratified fluid over topography. *J. Fluid Mech.* **169**, 429.

Holyer, J. Y. 1979 Large amplitude progressive interfacial waves. *J. Fluid Mech.* **93**, 433.

Joseph, R. I. 1977 Solitary waves in a finite depth fluid. *J. Phys.* A: *Math. Gen.* **10**, L225.

Keulegan, G. H. 1953 Characteristics of internal solitary waves. *J. Res. Natl Bur. Stand.* **51**, 133.

Koop, C. G. & Butler, G. 1981 An investigation on internal solitary waves in a two-fluid system. *J. Fluid Mech.* **112**, 225.

Kubota, T., Ko, D. R. S. & Dobbs, L. D. 1978 Weakly-nonlinear, long internal gravity waves in stratified fluids of finite depth. *J. Hydronaut.* **12**, 157.

Long, R. R. 1956 Solitary waves in one and two fluid systems. *Tellus* **8**, 460.

Meiron, D. I. & Saffman, P. G. 1983 Overhanging interfacial garvity waves of large amplitude. *J. Fluid Mech.* **120**, 213.

Melville, W. K. & Helfrich, K. R. 1987 Transcritical two-layer flow over topography. *J. Fluid Mech.* **178**, 31 (referred to herein as MH).

Miles, J. W. 1979 On internal solitary waves. *Tellus* **31**, 456.

Miles, J. W. 1981 On internal solitary waves II. *Tellus* **33**, 397.

Ono, H. 1975 Algebraic solitary waves in stratified fluids. *J. Phys. Soc. Japan* **39**, 1082.

Pullin, D. I. & Grimshaw, R. H. J. 1988 Finite-amplitude solitary waves at the interface between two homogeneous fluids. *Phys. Fluids* **31**, 3550.

Roberts, A. J. 1983 A stable and accurate numerical method to calculate the motion of a sharp interface between fluids. *IMA J. Appl. Math.* **31**, 31.

Schultz, W. W., Huh, J. & Griffin, O. M. 1994 Potential energy in steep and breaking waves. *J. Fluid Mech.* **278**, 201.

Segur, H. & Hammack, J. L. 1982 Soliton models of long internal waves. *J. Fluid Mech.* **118**, 285.

Shelley, M. J. 1992 A study of singularity formation in vortex-sheet motion by a spectrally accurate vortex method. *J. Fluid Mech.* **244**, 493.

Staquet, C. & Sommeria, J. 1996 Internal waves, turbulence and mixing in stratified flows: a report on Euromech Colloquium 339. *J. Fluid Mech.* **314**, 349.

Turner, R. E. L. & Vanden-Broeck, J.-M. 1986 The limiting configuration of interfacial gravity waves. *Phys. Fluids* **29**, 372.

Turner, R. E. L. & Vanden-Broeck, J.-M. 1988 Broadening of interfacial solitary waves. *Phys. Fluids* **31**, 2486.

Vanden-Broeck, J.-M. 1980 Numerical calculation of gravity-capillary interfacial waves of finite amplitude. *Phys. Fluids* **23**, 1723.

Vinje, T. & Brevig, P. 1981 Numerical simulation of breaking waves. *Adv. Water Res.* **4**, 77.

Wu, T. Y. 1987 Generation of upstream advancing solitons by moving disturbances. *J. Fluid Mech.* **184**, 75.

Zhou, Q.-N. & Graebel, W. P. 1990 Axisymmetric draining of a cylindrical tank with a free surface. *J. Fluid Mech.* **221**, 511.

Zhu, J., Wu, T. Y. & Yates, G. T. 1987 Internal solitary waves generated by moving disturbances. *3rd Intl Symp. on Stratified Flows, California Inst. of Tech., Pasadena, California, 3–5 February*, p. 1